

Optical coherence elastography – OCT at work in tissue biomechanics [Invited]

KIRILL V. LARIN^{1,2,5} AND DAVID D. SAMPSON^{3,4,6}

¹Department of Biomedical Engineering, University of Houston, 3605 Cullen Blvd., Houston, Texas 77204-5060, USA

²Department of Molecular Physiology and Biophysics, Baylor College of Medicine, 1 Baylor Plaza, Houston, Texas 77030, USA

³Optical + Biomedical Engineering Laboratory, School of Electrical, Electronic & Computer Engineering, The University of Western Australia, 35 Stirling Highway, Perth, WA 6009, Australia

⁴Centre for Microscopy, Characterisation & Analysis, The University of Western Australia, 35 Stirling Highway, Perth, WA 6009, Australia

⁵klarin@uh.edu

⁶David.Sampson@uwa.edu.au

Abstract: Optical coherence elastography (OCE), as the use of OCT to perform elastography has come to be known, began in 1998, around ten years after the rest of the field of elastography – the use of imaging to deduce mechanical properties of tissues. After a slow start, the maturation of OCT technology in the early to mid 2000s has underpinned a recent acceleration in the field. With more than 20 papers published in 2015, and more than 25 in 2016, OCE is growing fast, but still small compared to the companion fields of cell mechanics research methods, and medical elastography. In this review, we describe the early developments in OCE, and the factors that led to the current acceleration. Much of our attention is on the key recent advances, with a strong emphasis on future prospects, which are exceptionally bright.

© 2017 Optical Society of America

OCIS codes: (110.4500) Optical coherence tomography; (170.4500) Optical coherence tomography.

References and links

1. J. Schmitt, "OCT elastography: imaging microscopic deformation and strain of tissue," *Opt. Express* **3**(6), 199–211 (1998).
2. B. F. Kennedy, K. M. Kennedy, A. L. Oldenburg, S. G. Adie, S. A. Boppart, and D. D. Sampson, "Optical coherence elastography," in *Optical Coherence Tomography Technology and Applications*, Second ed., W. Drexler and J. G. Fujimoto, eds. (Springer, 2015), pp. 1007–1054.
3. R. W. Kirk, B. F. Kennedy, D. D. Sampson, and R. A. McLaughlin, "Near video-rate optical coherence elastography by acceleration with a graphics processing unit," *J. Lightwave Technol.* **33**(16), 3481–3485 (2015).
4. B. F. Kennedy, K. M. Kennedy, and D. D. Sampson, "A review of optical coherence elastography: Fundamentals, techniques and prospects," *IEEE J. Sel. Top. Quantum Electron.* **20**(2), 7101217 (2014).
5. S. Wang and K. V. Larin, "Optical coherence elastography for tissue characterization: a review," *J. Biophotonics* **8**(4), 279–302 (2015).
6. J. A. Mulligan, G. R. Untracht, S. N. Chandrasekaran, C. N. Brown, and S. G. Adie, "Emerging approaches for high-resolution imaging of tissue biomechanics with optical coherence elastography," *IEEE J. Sel. Top. Quantum Electron.* **22**(3), 6800520 (2016).
7. K. J. Parker, M. M. Doyley, and D. J. Rubens, "Imaging the elastic properties of tissue: the 20 year perspective," *Phys. Med. Biol.* **56**(1), R1–R29 (2011).
8. P. N. T. Wells and H. D. Liang, "Medical ultrasound: imaging of soft tissue strain and elasticity," *J. R. Soc. Interface* **8**(64), 1521–1549 (2011).
9. K. J. Glaser, A. Manduca, and R. L. Ehman, "Review of MR elastography applications and recent developments," *J. Magn. Reson. Imaging* **36**(4), 757–774 (2012).
10. R. Chan, A. Chau, W. Karl, S. Nadkarni, A. Khalil, N. Iftimia, M. Shishkov, G. Tearney, M. Kaazempur-Mofrad, and B. Bouma, "OCT-based arterial elastography: robust estimation exploiting tissue biomechanics," *Opt. Express* **12**(19), 4558–4572 (2004).
11. G. J. Tearney, E. Regar, T. Akasaka, T. Adriaenssens, P. Barlis, H. G. Bezerra, B. Bouma, N. Bruining, J. M. Cho, S. Chowdhary, M. A. Costa, R. de Silva, J. Dijkstra, C. Di Mario, D. Dudek, E. Falk, M. D. Feldman, P. Fitzgerald, H. M. Garcia-Garcia, N. Gonzalo, J. F. Granada, G. Guagliumi, N. R. Holm, Y. Honda, F. Ikeno, M. Kawasaki, J. Kochman, L. Koltowski, T. Kubo, T. Kume, H. Kyono, C. C. Lam, G. Lamouche, D. P. Lee, M. B.

- Leon, A. Maehara, O. Manfrini, G. S. Mintz, K. Mizuno, M. A. Morel, S. Nadkarni, H. Okura, H. Otake, A. Pietrasik, F. Prati, L. Räber, M. D. Radu, J. Rieber, M. Riga, A. Rollins, M. Rosenberg, V. Sirbu, P. W. Serruys, K. Shimada, T. Shinke, J. Shite, E. Siegel, S. Sonoda, M. Suter, S. Takarada, A. Tanaka, M. Terashima, T. Thim, S. Uemura, G. J. Ughi, H. M. van Beusekom, A. F. van der Steen, G. A. van Es, G. van Soest, R. Virmani, S. Waxman, N. J. Weissman, and G. Weisz; International Working Group for Intravascular Optical Coherence Tomography (IWG-IVOCT), "Consensus standards for acquisition, measurement, and reporting of intravascular optical coherence tomography studies: a report from the International Working Group for Intravascular Optical Coherence Tomography Standardization and Validation," *J. Am. Coll. Cardiol.* **59**(12), 1058–1072 (2012).
12. J. Rogowska, N. A. Patel, J. G. Fujimoto, and M. E. Brezinski, "Optical coherence tomographic elastography technique for measuring deformation and strain of atherosclerotic tissues," *Heart* **90**(5), 556–562 (2004).
 13. J. A. Schaar, C. L. De Korte, F. Mastik, C. Strijder, G. Pasterkamp, E. Boersma, P. W. Serruys, and A. F. W. Van Der Steen, "Characterizing vulnerable plaque features with intravascular elastography," *Circulation* **108**(21), 2636–2641 (2003).
 14. F. Deleaval, A. Bouvier, G. Finet, G. Cloutier, S. K. Yazdani, S. Le Floch, P. Clarysse, R. I. Pettigrew, and J. Ohayon, "The intravascular ultrasound elasticity-palpography technique revisited: a reliable tool for the in vivo detection of vulnerable coronary atherosclerotic plaques," *Ultrasound Med. Biol.* **39**(8), 1469–1481 (2013).
 15. A. H. Chau, R. C. Chan, M. Shishkov, B. MacNeill, N. Ifimia, G. J. Tearney, R. D. Kamm, B. E. Bouma, and M. R. Kaazempur-Mofrad, "Mechanical analysis of atherosclerotic plaques based on optical coherence tomography," *Ann. Biomed. Eng.* **32**(11), 1494–1503 (2004).
 16. A. S. Khalil, R. C. Chan, A. H. Chau, B. E. Bouma, and M. R. Kaazempur Mofrad, "Tissue elasticity estimation with optical coherence elastography: toward mechanical characterization of in vivo soft tissue," *Ann. Biomed. Eng.* **33**(11), 1631–1639 (2005).
 17. A. S. Khalil, B. E. Bouma, and M. R. Kaazempur Mofrad, "A combined FEM/genetic algorithm for vascular soft tissue elasticity estimation," *Cardiovasc. Eng.* **6**(3), 93–102 (2006).
 18. G. van Soest, F. Mastik, N. de Jong, and A. F. W. van der Steen, "Robust intravascular optical coherence elastography by line correlations," *Phys. Med. Biol.* **52**(9), 2445–2458 (2007).
 19. S. J. Kirkpatrick, R. K. Wang, and D. D. Duncan, "OCT-based elastography for large and small deformations," *Opt. Express* **14**(24), 11585–11597 (2006).
 20. I. Yamaguchi, "A laser-speckle strain-gauge," *J. Phys. E: Sci. Instrum.* **14**, 1270–1273 (1981).
 21. F. Hild and S. Roux, "Digital image correlation: from displacement measurement to identification of elastic properties - a review," *Strain* **42**(2), 69–80 (2006).
 22. B. Pan, K. M. Qian, H. M. Xie, and A. Asundi, "Two-dimensional digital image correlation for in-plane displacement and strain measurement: a review," *Meas. Sci. Technol.* **20**(6), 062001 (2009).
 23. H. J. Ko, W. Tan, R. Stack, and S. A. Boppart, "Optical coherence elastography of engineered and developing tissue," *Tissue Eng.* **12**(1), 63–73 (2006).
 24. R. Raghunathan, M. Singh, M. E. Dickinson, and K. V. Larin, "Optical coherence tomography for embryonic imaging: a review," *J. Biomed. Opt.* **21**(5), 050902 (2016).
 25. Z. Chen, T. E. Milner, S. Srinivas, X. Wang, A. Malekafzali, M. J. C. van Gemert, and J. S. Nelson, "Noninvasive imaging of in vivo blood flow velocity using optical Doppler tomography," *Opt. Lett.* **22**(14), 1119–1121 (1997).
 26. J. A. Izatt, M. D. Kulkarni, S. Yazdanfar, J. K. Barton, and A. J. Welch, "In vivo bidirectional color Doppler flow imaging of picoliter blood volumes using optical coherence tomography," *Opt. Lett.* **22**(18), 1439–1441 (1997).
 27. D. Uttam and B. Culshaw, "Precision time domain reflectometry in optical fiber systems using a frequency modulated continuous wave ranging technique," *J. Lightwave Technol.* **3**(5), 971–977 (1985).
 28. E. D. J. Smith, S. C. Moore, N. Wada, W. Chujo, and D. D. Sampson, "Spectral domain interferometry for OADR using non-Gaussian broad-band sources," *IEEE Photonics Technol. Lett.* **13**(1), 64–66 (2001).
 29. A. V. Zvyagin, E. D. J. Smith, and D. D. Sampson, "Delay and dispersion characteristics of a frequency-domain optical delay line for scanning interferometry," *J. Opt. Soc. Am. A* **20**(2), 333–341 (2003).
 30. R. Leitgeb, C. Hitzenberger, and A. Fercher, "Performance of fourier domain vs. time domain optical coherence tomography," *Opt. Express* **11**(8), 889–894 (2003).
 31. J. F. de Boer, B. Cense, B. H. Park, M. C. Pierce, G. J. Tearney, and B. E. Bouma, "Improved signal-to-noise ratio in spectral-domain compared with time-domain optical coherence tomography," *Opt. Lett.* **28**(21), 2067–2069 (2003).
 32. M. Choma, M. Sarunic, C. Yang, and J. Izatt, "Sensitivity advantage of swept source and Fourier domain optical coherence tomography," *Opt. Express* **11**(18), 2183–2189 (2003).
 33. R. K. Wang, Z. H. Ma, and S. J. Kirkpatrick, "Tissue Doppler optical coherence elastography for real time strain rate and strain mapping of soft tissue," *Appl. Phys. Lett.* **89**(14), 144103 (2006).
 34. R. K. Wang, S. Kirkpatrick, and M. Hinds, "Phase-sensitive optical coherence elastography for mapping tissue microstrains in real time," *Appl. Phys. Lett.* **90**(16), 164105 (2007).
 35. X. Liang, V. Crecea, and S. A. Boppart, "Dynamic optical coherence elastography: A review," *J. Innov. Opt. Health Sci.* **3**(4), 221–233 (2010).
 36. C. Sun, B. Standish, and V. X. D. Yang, "Optical coherence elastography: current status and future applications," *J. Biomed. Opt.* **16**(4), 043001 (2011).

37. K. M. Kennedy, S. Es'haghian, L. Chin, R. A. McLaughlin, D. D. Sampson, and B. F. Kennedy, "Optical palpation: optical coherence tomography-based tactile imaging using a compliant sensor," *Opt. Lett.* **39**(10), 3014–3017 (2014).
38. S. G. Adie, X. Liang, B. F. Kennedy, R. John, D. D. Sampson, and S. A. Boppart, "Spectroscopic optical coherence elastography," *Opt. Express* **18**(25), 25519–25534 (2010).
39. N. Özkaya, M. Nordin, D. Goldsheyder, and D. Leger, *Fundamentals of Biomechanics: Equilibrium, Motion, and Deformation* (Springer-Verlag, New York, 2012).
40. M. Orescanin, K. S. Toohy, and M. F. Insana, "Material properties from acoustic radiation force step response," *J. Acoust. Soc. Am.* **125**(5), 2928–2936 (2009).
41. X. Liang, A. L. Oldenburg, V. Crecea, E. J. Chaney, and S. A. Boppart, "Optical micro-scale mapping of dynamic biomechanical tissue properties," *Opt. Express* **16**(15), 11052–11065 (2008).
42. I. Z. Nenadic, M. W. Urban, S. A. Mitchell, and J. F. Greenleaf, "Lamb wave dispersion ultrasound vibrometry (LDUV) method for quantifying mechanical properties of viscoelastic solids," *Phys. Med. Biol.* **56**(7), 2245–2264 (2011).
43. I. Z. Nenadic, M. W. Urban, S. Aristizabal, S. A. Mitchell, T. C. Humphrey, and J. F. Greenleaf, "On Lamb and Rayleigh wave convergence in viscoelastic tissues," *Phys. Med. Biol.* **56**(20), 6723–6738 (2011).
44. J. F. Doyle, *Wave Propagation in Structures* (Springer-Verlag, New York, 1997).
45. Z. Han, J. Li, M. Singh, C. Wu, C. H. Liu, S. Wang, R. Idugboe, R. Raghunathan, N. Sudheendran, S. R. Aglyamov, M. D. Twa, and K. V. Larin, "Quantitative methods for reconstructing tissue biomechanical properties in optical coherence elastography: a comparison study," *Phys. Med. Biol.* **60**(9), 3531–3547 (2015).
46. C. Sun, B. Standish, B. Vuong, X. Y. Wen, and V. Yang, "Digital image correlation-based optical coherence elastography," *J. Biomed. Opt.* **18**(12), 121515 (2013).
47. L. Chin, A. Curatolo, B. F. Kennedy, B. J. Doyle, P. R. T. Munro, R. A. McLaughlin, and D. D. Sampson, "Analysis of image formation in optical coherence elastography using a multiphysics approach," *Biomed. Opt. Express* **5**(9), 2913–2930 (2014).
48. M. Sticker, C. K. Hitzengerger, R. Leitgeb, and A. F. Fercher, "Quantitative differential phase measurement and imaging in transparent and turbid media by optical coherence tomography," *Opt. Lett.* **26**(8), 518–520 (2001).
49. R. K. Manapuram, S. A. Baranov, V. G. R. Manne, N. Sudheendran, M. Mashiatulla, S. Aglyamov, S. Emelianov, and K. V. Larin, "Assessment of wave propagation on surfaces of crystalline lens with phase sensitive optical coherence tomography," *Laser Phys. Lett.* **8**(2), 164–168 (2011).
50. B. Park, M. C. Pierce, B. Cense, S. H. Yun, M. Mujat, G. Tearney, B. Bouma, and J. de Boer, "Real-time fiber-based multi-functional spectral-domain optical coherence tomography at 1.3 μm ," *Opt. Express* **13**(11), 3931–3944 (2005).
51. B. Vakoc, S. Yun, J. de Boer, G. Tearney, and B. Bouma, "Phase-resolved optical frequency domain imaging," *Opt. Express* **13**(14), 5483–5493 (2005).
52. B. F. Kennedy, R. A. McLaughlin, K. M. Kennedy, L. Chin, A. Curatolo, A. Tien, B. Latham, C. M. Saunders, and D. D. Sampson, "Optical coherence micro-elastography: mechanical-contrast imaging of tissue microstructure," *Biomed. Opt. Express* **5**(7), 2113–2124 (2014).
53. B. F. Kennedy, S. H. Koh, R. A. McLaughlin, K. M. Kennedy, P. R. T. Munro, and D. D. Sampson, "Strain estimation in phase-sensitive optical coherence elastography," *Biomed. Opt. Express* **3**(8), 1865–1879 (2012).
54. K. M. Kennedy, L. Chin, R. A. McLaughlin, B. Latham, C. M. Saunders, D. D. Sampson, and B. F. Kennedy, "Quantitative micro-elastography: imaging of tissue elasticity using compression optical coherence elastography," *Sci. Rep.* **5**, 15538 (2015).
55. V. Y. Zaitsev, A. L. Matveyev, L. A. Matveev, G. V. Gelikonov, A. I. Omelchenko, D. V. Shabanov, O. I. Baum, V. M. Svistushkin, and E. N. Sobol, "Optical coherence tomography for visualizing transient strains and measuring large deformations in laser-induced tissue reshaping," *Laser Phys. Lett.* **13**(11), 115603 (2016).
56. S. Song, Z. Huang, and R. K. Wang, "Tracking mechanical wave propagation within tissue using phase-sensitive optical coherence tomography: motion artifact and its compensation," *J. Biomed. Opt.* **18**(12), 121505 (2013).
57. S. Wang and K. V. Larin, "Noncontact depth-resolved micro-scale optical coherence elastography of the cornea," *Biomed. Opt. Express* **5**(11), 3807–3821 (2014).
58. K. Kurokawa, S. Makita, Y. J. Hong, and Y. Yasuno, "In-plane and out-of-plane tissue micro-displacement measurement by correlation coefficients of optical coherence tomography," *Opt. Lett.* **40**(9), 2153–2156 (2015).
59. K. Kurokawa, S. Makita, Y. J. Hong, and Y. Yasuno, "Two-dimensional micro-displacement measurement for laser coagulation using optical coherence tomography," *Biomed. Opt. Express* **6**(1), 170–190 (2015).
60. V. Y. Zaitsev, A. L. Matveyev, L. A. Matveev, G. V. Gelikonov, E. V. Gubarkova, N. D. Gladkova, and A. Vitkin, "Hybrid method of strain estimation in optical coherence elastography using combined sub-wavelength phase measurements and supra-pixel displacement tracking," *J. Biophotonics* **9**(5), 499–509 (2016).
61. G. Liu, L. Chou, W. Jia, W. Qi, B. Choi, and Z. Chen, "Intensity-based modified Doppler variance algorithm: application to phase instable and phase stable optical coherence tomography systems," *Opt. Express* **19**(12), 11429–11440 (2011).
62. J. Zhu, Y. Qu, T. Ma, R. Li, Y. Du, S. Huang, K. K. Shung, Q. Zhou, and Z. Chen, "Imaging and characterizing shear wave and shear modulus under orthogonal acoustic radiation force excitation using OCT Doppler variance method," *Opt. Lett.* **40**(9), 2099–2102 (2015).

63. Z. Han, S. R. Aglyamov, J. Li, M. Singh, S. Wang, S. Vantipalli, C. Wu, C. H. Liu, M. D. Twa, and K. V. Larin, "Quantitative assessment of corneal viscoelasticity using optical coherence elastography and a modified Rayleigh-Lamb equation," *J. Biomed. Opt.* **20**(2), 020501 (2015).
64. S. R. Aglyamov, S. Wang, A. B. Karpiouk, J. Li, M. Twa, S. Y. Emelianov, and K. V. Larin, "The dynamic deformation of a layered viscoelastic medium under surface excitation," *Phys. Med. Biol.* **60**(11), 4295–4312 (2015).
65. M. R. Ford, W. J. Dupps, Jr., A. M. Rollins, A. S. Roy, and Z. Hu, "Method for optical coherence elastography of the cornea," *J. Biomed. Opt.* **16**(1), 016005 (2011).
66. B. K. Armstrong, M. P. Lin, M. R. Ford, M. R. Santhiago, V. Singh, G. H. Grossman, V. Agrawal, A. S. Roy, R. S. Butler, W. J. Dupps, and S. E. Wilson, "Biological and biomechanical responses to traditional epithelium-off and transepithelial riboflavin-UVA CXL techniques in rabbits," *J. Refract. Surg.* **29**(5), 332–341 (2013).
67. M. R. Ford, A. S. Roy, A. M. Rollins, and W. J. Dupps, Jr., "Serial biomechanical comparison of edematous, normal, and collagen crosslinked human donor corneas using optical coherence elastography," *J. Cataract Refract. Surg.* **40**(6), 1041–1047 (2014).
68. A. A. M. Torricelli, M. R. Ford, V. Singh, M. R. Santhiago, W. J. Dupps, Jr., and S. E. Wilson, "BAC-EDTA transepithelial riboflavin-UVA crosslinking has greater biomechanical stiffening effect than standard epithelium-off in rabbit corneas," *Exp. Eye Res.* **125**, 114–117 (2014).
69. K. M. Kennedy, B. F. Kennedy, R. A. McLaughlin, and D. D. Sampson, "Needle optical coherence elastography for tissue boundary detection," *Opt. Lett.* **37**(12), 2310–2312 (2012).
70. X. Liang and S. A. Boppart, "Biomechanical properties of in vivo human skin from dynamic optical coherence elastography," *IEEE Trans. Biomed. Eng.* **57**(4), 953–959 (2010).
71. C. Li, G. Guan, R. Reif, Z. Huang, and R. K. Wang, "Determining elastic properties of skin by measuring surface waves from an impulse mechanical stimulus using phase-sensitive optical coherence tomography," *J. R. Soc. Interface* **9**(70), 831–841 (2012).
72. R. K. Manapuram, S. R. Aglyamov, F. M. Monediado, M. Mashiatulla, J. Li, S. Y. Emelianov, and K. V. Larin, "In vivo estimation of elastic wave parameters using phase-stabilized swept source optical coherence elastography," *J. Biomed. Opt.* **17**(10), 100501 (2012).
73. K. M. Kennedy, R. A. McLaughlin, B. F. Kennedy, A. Tien, B. Latham, C. M. Saunders, and D. D. Sampson, "Needle optical coherence elastography for the measurement of microscale mechanical contrast deep within human breast tissues," *J. Biomed. Opt.* **18**(12), 121510 (2013).
74. D. Chavan, J. Mo, M. de Groot, A. Meijering, J. F. de Boer, and D. Iannuzzi, "Collecting optical coherence elastography depth profiles with a micromachined cantilever probe," *Opt. Lett.* **38**(9), 1476–1478 (2013).
75. Y. P. Huang, Y. P. Zheng, S. Z. Wang, Z. P. Chen, Q. H. Huang, and Y. H. He, "An optical coherence tomography (OCT)-based air jet indentation system for measuring the mechanical properties of soft tissues," *Meas. Sci. Technol.* **20**(1), 1–11 (2009).
76. D. Alonso-Caneiro, K. Karnowski, B. J. Kaluzny, A. Kowalczyk, and M. Wojtkowski, "Assessment of corneal dynamics with high-speed swept source optical coherence tomography combined with an air puff system," *Opt. Express* **19**(15), 14188–14199 (2011).
77. C. Dorronsoro, D. Pascual, P. Pérez-Merino, S. Kling, and S. Marcos, "Dynamic OCT measurement of corneal deformation by an air puff in normal and cross-linked corneas," *Biomed. Opt. Express* **3**(3), 473–487 (2012).
78. S. G. Adie, B. F. Kennedy, J. J. Armstrong, S. A. Alexandrov, and D. D. Sampson, "Audio frequency in vivo optical coherence elastography," *Phys. Med. Biol.* **54**(10), 3129–3139 (2009).
79. E. W. Chang, J. B. Kobler, and S. H. Yun, "Subnanometer optical coherence tomographic vibrography," *Opt. Lett.* **37**(17), 3678–3680 (2012).
80. B. I. Akca, E. W. Chang, S. Kling, A. Ramier, G. Scarcelli, S. Marcos, and S. H. Yun, "Observation of sound-induced corneal vibrational modes by optical coherence tomography," *Biomed. Opt. Express* **6**(9), 3313–3319 (2015).
81. S. Wang, K. V. Larin, J. S. Li, S. Vantipalli, R. K. Manapuram, S. Aglyamov, S. Emelianov, and M. D. Twa, "A focused air-pulse system for optical-coherence-tomography-based measurements of tissue elasticity," *Laser Phys. Lett.* **10**(7), 075605 (2013).
82. A. P. Sarvazyan, O. V. Rudenko, S. D. Swanson, J. B. Fowlkes, and S. Y. Emelianov, "Shear wave elasticity imaging: a new ultrasonic technology of medical diagnostics," *Ultrasound Med. Biol.* **24**(9), 1419–1435 (1998).
83. X. Liang, M. Orescanin, K. S. Toohey, M. F. Insana, and S. A. Boppart, "Acoustomotive optical coherence elastography for measuring material mechanical properties," *Opt. Lett.* **34**(19), 2894–2896 (2009).
84. W. Qi, R. Chen, L. Chou, G. Liu, J. Zhang, Q. Zhou, and Z. Chen, "Phase-resolved acoustic radiation force optical coherence elastography," *J. Biomed. Opt.* **17**(11), 110505 (2012).
85. O. A. Ejofodomi, V. Zderic, and J. M. Zara, "Development of novel imaging probe for optical/acoustic radiation imaging (OARI)," *Med. Phys.* **40**(11), 111910 (2013).
86. G. Guan, C. Li, Y. Ling, Y. Yang, J. B. Vorstius, R. P. Keatch, R. K. Wang, and Z. Huang, "Quantitative evaluation of degenerated tendon model using combined optical coherence elastography and acoustic radiation force method," *J. Biomed. Opt.* **18**(11), 111417 (2013).
87. S. Wang, S. Aglyamov, A. Karpiouk, J. Li, S. Emelianov, F. Manns, and K. V. Larin, "Assessing the mechanical properties of tissue-mimicking phantoms at different depths as an approach to measure biomechanical gradient of crystalline lens," *Biomed. Opt. Express* **4**(12), 2769–2780 (2013).

88. M. Razani, A. Mariampillai, C. Sun, T. W. H. Luk, V. X. D. Yang, and M. C. Kolios, "Feasibility of optical coherence elastography measurements of shear wave propagation in homogeneous tissue equivalent phantoms," *Biomed. Opt. Express* **3**(5), 972–980 (2012).
89. M. Razani, T. W. H. Luk, A. Mariampillai, P. Siegler, T. R. Kiehl, M. C. Kolios, and V. X. D. Yang, "Optical coherence tomography detection of shear wave propagation in inhomogeneous tissue equivalent phantoms and ex-vivo carotid artery samples," *Biomed. Opt. Express* **5**(3), 895–906 (2014).
90. T. M. Nguyen, S. Song, B. Arnal, Z. Huang, M. O'Donnell, and R. K. Wang, "Visualizing ultrasonically induced shear wave propagation using phase-sensitive optical coherence tomography for dynamic elastography," *Opt. Lett.* **39**(4), 838–841 (2014).
91. W. Qi, R. Li, T. Ma, J. Li, K. Kirk Shung, Q. Zhou, and Z. Chen, "Resonant acoustic radiation force optical coherence elastography," *Appl. Phys. Lett.* **103**(10), 103704 (2013).
92. X. Xu, J. Zhu, and Z. Chen, "Dynamic and quantitative assessment of blood coagulation using optical coherence elastography," *Sci. Rep.* **6**, 24294 (2016).
93. W. Qi, R. Li, T. Ma, K. Kirk Shung, Q. Zhou, and Z. Chen, "Confocal acoustic radiation force optical coherence elastography using a ring ultrasonic transducer," *Appl. Phys. Lett.* **104**(12), 123702 (2014).
94. T. M. Nguyen, B. Arnal, S. Song, Z. Huang, R. K. Wang, and M. O'Donnell, "Shear wave elastography using amplitude-modulated acoustic radiation force and phase-sensitive optical coherence tomography," *J. Biomed. Opt.* **20**(1), 016001 (2015).
95. Ł. Ambroziński, I. Pelivanov, S. Song, S. J. Yoon, D. Li, L. Gao, T. T. Shen, R. K. Wang, and M. O'Donnell, "Air-coupled acoustic radiation force for non-contact generation of broadband mechanical waves in soft media," *Appl. Phys. Lett.* **109**(4), 043701 (2016).
96. Ł. Ambroziński, S. Song, S. J. Yoon, I. Pelivanov, D. Li, L. Gao, T. T. Shen, R. K. Wang, and M. O'Donnell, "Acoustic micro-tapping for non-contact 4D imaging of tissue elasticity," *Sci. Rep.* **6**, 38967 (2016).
97. S. Wang, J. Li, R. K. Manapuram, F. M. Menodiado, D. R. Ingram, M. D. Twa, A. J. Lazar, D. C. Lev, R. E. Pollock, and K. V. Larin, "Noncontact measurement of elasticity for the detection of soft-tissue tumors using phase-sensitive optical coherence tomography combined with a focused air-puff system," *Opt. Lett.* **37**(24), 5184–5186 (2012).
98. J. Li, S. Wang, R. K. Manapuram, M. Singh, F. M. Menodiado, S. Aglyamov, S. Emelianov, M. D. Twa, and K. V. Larin, "Dynamic optical coherence tomography measurements of elastic wave propagation in tissue-mimicking phantoms and mouse cornea in vivo," *J. Biomed. Opt.* **18**(12), 121503 (2013).
99. J. Li, Z. Han, M. Singh, M. D. Twa, and K. V. Larin, "Differentiating untreated and cross-linked porcine corneas of the same measured stiffness with optical coherence elastography," *J. Biomed. Opt.* **19**(11), 110502 (2014).
100. J. S. Li, S. Wang, M. Singh, S. Aglyamov, S. Emelianov, M. D. Twa, and K. V. Larin, "Air-pulse OCE for assessment of age-related changes in mouse cornea in vivo," *Laser Phys. Lett.* **11**(6), 065601 (2014).
101. C. H. Liu, M. N. Skryabina, J. Li, M. Singh, E. N. Sobol, and K. V. Larin, "Measurement of the temperature dependence of Young's modulus of cartilage by phase-sensitive optical coherence elastography," *Quantum Electron.* **44**(8), 751–756 (2014).
102. M. D. Twa, J. Li, S. Vantipalli, M. Singh, S. Aglyamov, S. Emelianov, and K. V. Larin, "Spatial characterization of corneal biomechanical properties with optical coherence elastography after UV cross-linking," *Biomed. Opt. Express* **5**(5), 1419–1427 (2014).
103. S. Wang and K. V. Larin, "Shear wave imaging optical coherence tomography (SWI-OCT) for ocular tissue biomechanics," *Opt. Lett.* **39**(1), 41–44 (2014).
104. S. Wang, A. L. Lopez 3rd, Y. Morikawa, G. Tao, J. Li, I. V. Larina, J. F. Martin, and K. V. Larin, "Noncontact quantitative biomechanical characterization of cardiac muscle using shear wave imaging optical coherence tomography," *Biomed. Opt. Express* **5**(7), 1980–1992 (2014).
105. Z. Han, J. Li, M. Singh, S. R. Aglyamov, C. Wu, C. H. Liu, and K. V. Larin, "Analysis of the effects of curvature and thickness on elastic wave velocity in cornea-like structures by finite element modeling and optical coherence elastography," *Appl. Phys. Lett.* **106**(23), 233702 (2015).
106. C. H. Liu, M. Singh, J. S. Li, Z. L. Han, C. Wu, S. Wang, R. Idugboe, R. Raghunathan, E. N. Sobol, V. V. Tuchin, M. Twa, and K. V. Larin, "Quantitative assessment of hyaline cartilage elasticity during optical clearing using optical coherence elastography," *Sovrem. Tehnol. Med.* **7**(1), 44–51 (2015).
107. M. Singh, C. Wu, C. H. Liu, J. Li, A. Schill, A. Nair, and K. V. Larin, "Phase-sensitive optical coherence elastography at 1.5 million A-Lines per second," *Opt. Lett.* **40**(11), 2588–2591 (2015).
108. Y. Du, C. H. Liu, L. Lei, M. Singh, J. Li, M. J. Hicks, K. V. Larin, and C. Mohan, "Rapid, noninvasive quantitation of skin disease in systemic sclerosis using optical coherence elastography," *J. Biomed. Opt.* **21**(4), 046002 (2016).
109. Z. Han, J. Li, M. Singh, C. Wu, C. H. Liu, R. Raghunathan, S. R. Aglyamov, S. Vantipalli, M. D. Twa, and K. V. Larin, "Optical coherence elastography assessment of corneal viscoelasticity with a modified Rayleigh-Lamb wave model," *J. Mech. Behav. Biomed. Mater.* **66**, 87–94 (2017).
110. Z. Han, M. Singh, S. R. Aglyamov, C. H. Liu, A. Nair, R. Raghunathan, C. Wu, J. Li, and K. V. Larin, "Quantifying tissue viscoelasticity using optical coherence elastography and the Rayleigh wave model," *J. Biomed. Opt.* **21**(9), 090504 (2016).
111. Z. L. Han, J. S. Li, M. Singh, S. Vantipalli, S. R. Aglyamov, C. Wu, C. H. Liu, R. Raghunathan, M. D. Twa, and K. V. Larin, "Analysis of the effect of the fluid-structure interface on elastic wave velocity in cornea-like structures by OCE and FEM," *Laser Phys. Lett.* **13**(3), 035602 (2016).

112. C. H. Liu, Y. Du, M. Singh, C. Wu, Z. Han, J. Li, A. Chang, C. Mohan, and K. V. Larin, "Classifying murine glomerulonephritis using optical coherence tomography and optical coherence elastography," *J. Biophotonics* **9**(8), 781–791 (2016).
113. M. Singh, J. Li, Z. Han, S. Vantipalli, C. H. Liu, C. Wu, R. Raghunathan, S. R. Aglyamov, M. D. Twa, and K. V. Larin, "Evaluating the effects of riboflavin/UV-A and Rose-Bengal/green light cross-linking of the rabbit cornea by noncontact optical coherence elastography," *Invest. Ophthalmol. Vis. Sci.* **57**(9), OCT112 (2016).
114. M. Singh, J. Li, Z. Han, C. Wu, S. R. Aglyamov, M. D. Twa, and K. V. Larin, "Investigating elastic anisotropy of the porcine cornea as a function of intraocular pressure with optical coherence elastography," *J. Refract. Surg.* **32**(8), 562–567 (2016).
115. M. Singh, J. Li, S. Vantipalli, S. Wang, Z. Han, A. Nair, S. R. Aglyamov, M. D. Twa, and K. V. Larin, "Noncontact elastic wave imaging optical coherence elastography for evaluating changes in corneal elasticity due to crosslinking," *IEEE J. Sel. Top. Quantum Electron.* **22**(3), 6801911 (2016).
116. M. Singh, S. Wang, R. W. Yee, and K. V. Larin, "Optical coherence tomography as a tool for real-time visual feedback and biomechanical assessment of dermal filler injections: preliminary results in a pig skin model," *Exp. Dermatol.* **25**(6), 475–476 (2016).
117. C. Li, Z. Huang, and R. K. Wang, "Elastic properties of soft tissue-mimicking phantoms assessed by combined use of laser ultrasonics and low coherence interferometry," *Opt. Express* **19**(11), 10153–10163 (2011).
118. C. Li, G. Guan, Z. Huang, M. Johnstone, and R. K. Wang, "Noncontact all-optical measurement of corneal elasticity," *Opt. Lett.* **37**(10), 1625–1627 (2012).
119. C. Li, G. Guan, F. Zhang, S. Song, R. K. Wang, Z. Huang, and G. Nabi, "Quantitative elasticity measurement of urinary bladder wall using laser-induced surface acoustic waves," *Biomed. Opt. Express* **5**(12), 4313–4328 (2014).
120. C. Li, G. Guan, F. Zhang, G. Nabi, R. K. Wang, and Z. Huang, "Laser induced surface acoustic wave combined with phase sensitive optical coherence tomography for superficial tissue characterization: a solution for practical application," *Biomed. Opt. Express* **5**(5), 1403–1419 (2014).
121. S. Song, W. Wei, B. Y. Hsieh, I. Pelivanov, T. T. Shen, M. O'Donnell, and R. K. Wang, "Strategies to improve phase-stability of ultrafast swept source optical coherence tomography for single shot imaging of transient mechanical waves at 16 kHz frame rate," *Appl. Phys. Lett.* **108**(19), 191104 (2016).
122. L. V. Wang and S. Hu, "Photoacoustic tomography: in vivo imaging from organelles to organs," *Science* **335**(6075), 1458–1462 (2012).
123. P. Hai, Y. Zhou, L. Gong, and L. V. Wang, "Quantitative photoacoustic elastography in humans," *J. Biomed. Opt.* **21**(6), 066011 (2016).
124. C. Wu, M. Singh, Z. L. Han, R. Raghunathan, C. H. Liu, J. S. Li, A. Schill, and K. V. Larin, "Lorentz force megahertz optical coherence elastography," *J. Biomed. Opt.* **21**(9), 090502 (2016).
125. V. Crecea, A. L. Oldenburg, X. Liang, T. S. Ralston, and S. A. Boppart, "Magnetomotive nanoparticle transducers for optical rheology of viscoelastic materials," *Opt. Express* **17**(25), 23114–23122 (2009).
126. R. John, E. J. Chaney, and S. A. Boppart, "Dynamics of magnetic nanoparticle-based contrast agents in tissues tracked using magnetomotive optical coherence tomography," *IEEE J. Sel. Top. Quantum Electron.* **16**(3), 671–697 (2009).
127. R. John, R. Rezaeipoor, S. G. Adie, E. J. Chaney, A. L. Oldenburg, M. Marjanovic, J. P. Haldar, B. P. Sutton, and S. A. Boppart, "In vivo magnetomotive optical molecular imaging using targeted magnetic nanoprobe," *Proc. Natl. Acad. Sci. U.S.A.* **107**(18), 8085–8090 (2010).
128. A. L. Oldenburg and S. A. Boppart, "Resonant acoustic spectroscopy of soft tissues using embedded magnetomotive nanotransducers and optical coherence tomography," *Phys. Med. Biol.* **55**(4), 1189–1201 (2010).
129. J. Koo, C. Lee, H. W. Kang, Y. W. Lee, J. Kim, and J. Oh, "Pulsed magneto-motive optical coherence tomography for remote cellular imaging," *Opt. Lett.* **37**(17), 3714–3716 (2012).
130. A. L. Oldenburg, G. Wu, D. Spivak, F. Tsui, A. S. Wolberg, and T. H. Fischer, "Magnetomotive optical coherence tomography and labeled platelets," *IEEE J. Sel. Top. Quantum Electron.* **18**(3), 1100–1109 (2012).
131. V. Crecea, A. Ahmad, and S. A. Boppart, "Magnetomotive optical coherence elastography for microrheology of biological tissues," *J. Biomed. Opt.* **18**(12), 121504 (2013).
132. J. Kim, A. Ahmad, and S. A. Boppart, "Dual-coil magnetomotive optical coherence tomography for contrast enhancement in liquids," *Opt. Express* **21**(6), 7139–7147 (2013).
133. A. Ahmad, J. Kim, N. A. Sobh, N. D. Shemonski, and S. A. Boppart, "Magnetomotive optical coherence elastography using magnetic particles to induce mechanical waves," *Biomed. Opt. Express* **5**(7), 2349–2361 (2014).
134. V. Crecea, B. W. Graf, T. Kim, G. Popescu, and S. A. Boppart, "High resolution phase-sensitive magnetomotive optical coherence microscopy for tracking magnetic microbeads and cellular mechanics," *IEEE J. Sel. Top. Quantum Electron.* **20**(2), 6800907 (2014).
135. A. Ahmad, J. Kim, N. D. Shemonski, M. Marjanovic, and S. A. Boppart, "Volumetric full-range magnetomotive optical coherence tomography," *J. Biomed. Opt.* **19**(12), 126001 (2014).
136. J. Kim, A. Ahmad, M. Marjanovic, E. J. Chaney, J. Li, J. Rasio, Z. Hubler, D. Spillman, K. S. Suslick, and S. A. Boppart, "Magnetomotive optical coherence tomography for the assessment of atherosclerotic lesions using $\alpha\text{v}\beta 3$ integrin-targeted microspheres," *Mol. Imaging Biol.* **16**(1), 36–43 (2014).
137. A. Ahmad, P. C. Huang, N. A. Sobh, P. Pande, J. Kim, and S. A. Boppart, "Mechanical contrast in spectroscopic magnetomotive optical coherence elastography," *Phys. Med. Biol.* **60**(17), 6655–6668 (2015).

138. J. Kim, A. Ahmad, J. Li, M. Marjanovic, E. J. Chaney, K. S. Suslick, and S. A. Boppart, "Intravascular magnetomotive optical coherence tomography of targeted early-stage atherosclerotic changes in ex vivo hyperlipidemic rabbit aortas," *J. Biophotonics* **9**(1-2), 109–116 (2016).
139. P. C. Huang, P. Pande, A. Ahmad, M. Marjanovic, D. R. Spillman, B. Odintsov, and S. A. Boppart, "Magnetomotive optical coherence elastography for magnetic hyperthermia dosimetry based on dynamic tissue biomechanics," *IEEE J. Sel. Top. Quantum Electron.* **22**(4), 6802816 (2016).
140. G. Scarcelli and S. H. Yun, "Confocal Brillouin microscopy for three-dimensional mechanical imaging," *Nat. Photonics* **2**(1), 39–43 (2008).
141. J. I. Davies and A. D. Struthers, "Pulse wave analysis and pulse wave velocity: a critical review of their strengths and weaknesses," *J. Hypertens.* **21**(3), 463–472 (2003).
142. A. N. Gurovich and R. W. Braith, "Pulse wave analysis and pulse wave velocity techniques: are they ready for the clinic?" *Hypertens. Res.* **34**(2), 166–169 (2011).
143. P. Li, A. Liu, L. Shi, X. Yin, S. Rugonyi, and R. K. Wang, "Assessment of strain and strain rate in embryonic chick heart in vivo using tissue Doppler optical coherence tomography," *Phys. Med. Biol.* **56**(22), 7081–7092 (2011).
144. U. Bae, M. Dighe, T. Dubinsky, S. Minoshima, V. Shamdasani, and Y. Kim, "Ultrasound thyroid elastography using carotid artery pulsation: preliminary study," *J. Ultrasound Med.* **26**(6), 797–805 (2007).
145. J. B. Weaver, A. J. Pattison, M. D. McGarry, I. M. Perreard, J. G. Swienckowski, C. J. Eskey, S. S. Lollis, and K. D. Paulsen, "Brain mechanical property measurement using MRE with intrinsic activation," *Phys. Med. Biol.* **57**(22), 7275–7287 (2012).
146. P. J. McCracken, A. Manduca, J. Felmlee, and R. L. Ehman, "Mechanical transient-based magnetic resonance elastography," *Magn. Reson. Med.* **53**(3), 628–639 (2005).
147. J. Fu, M. Haghighi-Abayneh, F. Pierron, and P. D. Ruiz, "Depth-resolved full-field measurement of corneal deformation by optical coherence tomography and digital volume correlation," *Exp. Mech.* **56**(7), 1203–1217 (2016).
148. K. M. Kennedy, C. Ford, B. F. Kennedy, M. B. Bush, and D. D. Sampson, "Analysis of mechanical contrast in optical coherence elastography," *J. Biomed. Opt.* **18**(12), 121508 (2013).
149. A. Nahas, M. Bauer, S. Roux, and A. C. Boccara, "3D static elastography at the micrometer scale using Full Field OCT," *Biomed. Opt. Express* **4**(10), 2138–2149 (2013).
150. P. Wijesinghe, R. A. McLaughlin, D. D. Sampson, and B. F. Kennedy, "Parametric imaging of viscoelasticity using optical coherence elastography," *Phys. Med. Biol.* **60**(6), 2293–2307 (2015).
151. W. M. Allen, L. Chin, P. Wijesinghe, R. W. Kirk, B. Latham, D. D. Sampson, C. M. Saunders, and B. F. Kennedy, "Wide-field optical coherence micro-elastography for intraoperative assessment of human breast cancer margins," *Biomed. Opt. Express* **7**(10), 4139–4153 (2016).
152. R. A. McLaughlin, L. Scolaro, P. Robbins, C. Saunders, S. L. Jacques, and D. D. Sampson, "Parametric imaging of cancer with optical coherence tomography," *J. Biomed. Opt.* **15**(4), 046029 (2010).
153. L. Chin, B. F. Kennedy, K. M. Kennedy, P. Wijesinghe, G. J. Pinniger, J. R. Terrill, R. A. McLaughlin, and D. D. Sampson, "Three-dimensional optical coherence micro-elastography of skeletal muscle tissue," *Biomed. Opt. Express* **5**(9), 3090–3102 (2014).
154. K. M. Kennedy, L. Chin, P. Wijesinghe, R. A. McLaughlin, B. Latham, D. D. Sampson, C. M. Saunders, and B. F. Kennedy, "Investigation of optical coherence micro-elastography as a method to visualize micro-architecture in human axillary lymph nodes," *BMC Cancer* **16**(1), 874 (2016).
155. B. F. Kennedy, R. A. McLaughlin, K. M. Kennedy, L. Chin, P. Wijesinghe, A. Curatolo, A. Tien, M. Ronald, B. Latham, C. M. Saunders, and D. D. Sampson, "Investigation of optical coherence microelastography as a method to visualize cancers in human breast tissue," *Cancer Res.* **75**(16), 3236–3245 (2015).
156. E. D. Kurniawan, M. H. Wong, I. Windle, A. Rose, A. Mou, M. Buchanan, J. P. Collins, J. A. Miller, R. L. Gruen, and G. B. Mann, "Predictors of surgical margin status in breast-conserving surgery within a breast screening program," *Ann. Surg. Oncol.* **15**(9), 2542–2549 (2008).
157. R. Jeevan, D. A. Cromwell, M. Trivella, G. Lawrence, O. Kearins, J. Pereira, C. Sheppard, C. M. Caddy, and J. H. P. van der Meulen, "Reoperation rates after breast conserving surgery for breast cancer among women in England: retrospective study of hospital episode statistics," *BMJ* **345**, e4505 (2012).
158. M. Villiger, D. Lorensen, R. A. McLaughlin, B. C. Quirk, R. W. Kirk, B. E. Bouma, and D. D. Sampson, "Deep tissue volume imaging of birefringence through fibre-optic needle probes for the delineation of breast tumour," *Sci. Rep.* **6**, 28771 (2016).
159. L. Scolaro, R. A. McLaughlin, B. F. Kennedy, C. M. Saunders, and D. D. Sampson, "A review of optical coherence tomography in breast cancer," *Photonics Lasers Med.* **3**(3), 225–240 (2014).
160. A. Srivastava, Y. Verma, K. D. Rao, and P. K. Gupta, "Determination of elastic properties of resected human breast tissue samples using optical coherence tomographic elastography," *Strain* **47**(1), 75–87 (2011).
161. C. Zhou, D. W. Cohen, Y. Wang, H. C. Lee, A. E. Mondelblatt, T. H. Tsai, A. D. Aguirre, J. G. Fujimoto, and J. L. Connolly, "Integrated optical coherence tomography and microscopy for ex vivo multiscale evaluation of human breast tissues," *Cancer Res.* **70**(24), 10071–10079 (2010).
162. O. Assayag, M. Antoine, B. Sigal-Zafrani, M. Riben, F. Harms, A. Burcheri, K. Grieve, E. Dalimier, B. Le Conte de Poly, and C. Boccara, "Large field, high resolution full-field optical coherence tomography: a pre-clinical study of human breast tissue and cancer assessment," *Technol. Cancer Res. Treat.* **13**(5), 455–468 (2014).

163. S. J. Erickson-Bhatt, R. M. Nolan, N. D. Shemonski, S. G. Adie, J. Putney, D. Darga, D. T. McCormick, A. J. Cittadine, A. M. Zysk, M. Marjanovic, E. J. Chaney, G. L. Monroy, F. A. South, K. A. Craddock, Z. G. Liu, M. Sundaram, P. S. Ray, and S. A. Boppart, "Real-time imaging of the resection bed using a handheld probe to reduce incidence of microscopic positive margins in cancer surgery," *Cancer Res.* **75**(18), 3706–3712 (2015).
164. R. Li, P. Wang, L. Lan, F. P. Lloyd, Jr., C. J. Goergen, S. Chen, and J. X. Cheng, "Assessing breast tumor margin by multispectral photoacoustic tomography," *Biomed. Opt. Express* **6**(4), 1273–1281 (2015).
165. Y. Wang, S. Kang, A. Khan, G. Ruttner, S. Y. Leigh, M. Murray, S. Abeytunge, G. Peterson, M. Rajadhyaksha, S. Dintzis, S. Javid, and J. T. C. Liu, "Quantitative molecular phenotyping with topically applied SERS nanoparticles for intraoperative guidance of breast cancer lumpectomy," *Sci. Rep.* **6**, 21242 (2016).
166. J. Fu, F. Pierron, and P. D. Ruiz, "Elastic stiffness characterization using three-dimensional full-field deformation obtained with optical coherence tomography and digital volume correlation," *J. Biomed. Opt.* **18**(12), 121512 (2013).
167. V. Y. Zaitsev, A. L. Matveyev, L. A. Matveev, G. V. Gelikonov, V. M. Gelikonov, and A. Vitkin, "Deformation-induced speckle-pattern evolution and feasibility of correlational speckle tracking in optical coherence elastography," *J. Biomed. Opt.* **20**(7), 075006 (2015).
168. B. K. Bay, T. S. Smith, D. P. Fyhrrie, and M. Saad, "Digital volume correlation: Three-dimensional strain mapping using X-ray tomography," *Exp. Mech.* **39**(3), 217–226 (1999).
169. D. Zhang and D. D. Arola, "Applications of digital image correlation to biological tissues," *J. Biomed. Opt.* **9**(4), 691–699 (2004).
170. C. E. Leroux, J. Palmier, A. C. Boccara, G. Cappello, and S. Monnier, "Elastography of multicellular aggregates submitted to osmo-mechanical stress," *New J. Phys.* **17**(7), 073035 (2015).
171. A. Curatolo, M. Villiger, D. Lorensen, P. Wijesinghe, A. Fritz, B. F. Kennedy, and D. D. Sampson, "Ultrahigh-resolution optical coherence elastography," *Opt. Lett.* **41**(1), 21–24 (2016).
172. D. Pokharel, P. Wijesinghe, V. Oenarto, J. F. Lu, D. D. Sampson, B. F. Kennedy, V. P. Wallace, and M. Bebawy, "Deciphering cell-to-cell communication in acquisition of cancer traits: Extracellular membrane vesicles are regulators of tissue biomechanics," *OMICS* **20**(8), 462–469 (2016).
173. G. Y. H. Lee and C. T. Lim, "Biomechanics approaches to studying human diseases," *Trends Biotechnol.* **25**(3), 111–118 (2007).
174. T. A. Krouskop, T. M. Wheeler, F. Kallel, B. S. Garra, and T. Hall, "Elastic moduli of breast and prostate tissues under compression," *Ultrason. Imaging* **20**(4), 260–274 (1998).
175. R. Karimi, T. Zhu, B. E. Bouma, and M. R. Kaazempur Mofrad, "Estimation of nonlinear mechanical properties of vascular tissues via elastography," *Cardiovasc. Eng.* **8**(4), 191–202 (2008).
176. J. Rogowska, N. Patel, S. Plummer, and M. E. Brezinski, "Quantitative optical coherence tomographic elastography: method for assessing arterial mechanical properties," *Br. J. Radiol.* **79**(945), 707–711 (2006).
177. S. Es'haghian, K. M. Kennedy, P. Gong, D. D. Sampson, R. A. McLaughlin, and B. F. Kennedy, "Optical palpation in vivo: imaging human skin lesions using mechanical contrast," *J. Biomed. Opt.* **20**(1), 016013 (2015).
178. L. Dong, P. Wijesinghe, J. T. Dantuono, D. D. Sampson, P. R. T. Munro, B. F. Kennedy, and A. A. Oberai, "Quantitative optical coherence elastography as an inverse elasticity problem," *IEEE J. Sel. Top. Quantum Electron.* **22**(3), 6802211 (2016).
179. A. Manduca, T. E. Oliphant, M. A. Dresner, J. L. Mahowald, S. A. Kruse, E. Amromin, J. P. Felmlee, J. F. Greenleaf, and R. L. Ehman, "Magnetic resonance elastography: non-invasive mapping of tissue elasticity," *Med. Image Anal.* **5**(4), 237–254 (2001).
180. S. Song, Z. Huang, T. M. Nguyen, E. Y. Wong, B. Arnal, M. O'Donnell, and R. K. Wang, "Shear modulus imaging by direct visualization of propagating shear waves with phase-sensitive optical coherence tomography," *J. Biomed. Opt.* **18**(12), 121509 (2013).
181. K. F. Graff, *Wave Motion in Elastic Solids* (Dover Publications, New York, 2012).
182. K. D. Mohan and A. L. Oldenburg, "Elastography of soft materials and tissues by holographic imaging of surface acoustic waves," *Opt. Express* **20**(17), 18887–18897 (2012).
183. A. Nahas, M. Tanter, T. M. Nguyen, J. M. Chassot, M. Fink, and A. C. Boccara, "From supersonic shear wave imaging to full-field optical coherence shear wave elastography," *J. Biomed. Opt.* **18**(12), 121514 (2013).
184. C. H. Liu, A. Schill, C. Wu, M. Singh, and K. V. Larin, "Non-contact single shot elastography using line field low coherence holography," *Biomed. Opt. Express* **7**(8), 3021–3031 (2016).
185. P. Y. Chao and P. C. Li, "Three-dimensional shear wave imaging based on full-field laser speckle contrast imaging with one-dimensional mechanical scanning," *Opt. Express* **24**(17), 18860–18871 (2016).
186. S. Song, N. M. Le, Z. Huang, T. Shen, and R. K. Wang, "Quantitative shear-wave optical coherence elastography with a programmable phased array ultrasound as the wave source," *Opt. Lett.* **40**(21), 5007–5010 (2015).
187. M. Singh, J. Li, Z. Han, R. Raghunathan, A. Nair, C. Wu, C.-H. Liu, S. Aglyamov, M. D. Twa, and K. V. Larin, "Assessing the effects of riboflavin/UV-A crosslinking on porcine corneal mechanical anisotropy with optical coherence elastography," *Biomed. Opt. Express* **8**(1), 349–366 (2017).
188. M. Singh, J. Li, S. Vantipalli, Z. Han, K. V. Larin, and M. D. Twa, "Optical coherence elastography for evaluating customized riboflavin/UV-A corneal collagen crosslinking," *J. Biomed. Opt.* **22**(9), 091504 (2017).

- 189.C. Li, G. Guan, S. Li, Z. Huang, and R. K. Wang, "Evaluating elastic properties of heterogeneous soft tissue by surface acoustic waves detected by phase-sensitive optical coherence tomography," *J. Biomed. Opt.* **17**(5), 057002 (2012).
- 190.E. Soczkiewicz, "The penetration depth of the Rayleigh surface waves," *Nondestruct. Test. Eval.* **13**(2), 113–119 (1997).
- 191.C. Wu, Z. Han, S. Wang, J. Li, M. Singh, C. H. Liu, S. Aglyamov, S. Emelianov, F. Manns, and K. V. Larin, "Assessing age-related changes in the biomechanical properties of rabbit lens using a coaligned ultrasound and optical coherence elastography system," *Invest. Ophthalmol. Vis. Sci.* **56**(2), 1292–1300 (2015).
- 192.P. Meemon, J. Yao, Y. J. Chu, F. Zvietcovich, K. J. Parker, and J. P. Rolland, "Crawling wave optical coherence elastography," *Opt. Lett.* **41**(5), 847–850 (2016).
- 193.X. Liang, S. G. Adie, R. John, and S. A. Boppart, "Dynamic spectral-domain optical coherence elastography for tissue characterization," *Opt. Express* **18**(13), 14183–14190 (2010).
- 194.M. J. A. Girard, W. J. Dupps, M. Baskaran, G. Scarcelli, S. H. Yun, H. A. Quigley, I. A. Sigal, and N. G. Strouthidis, "Translating ocular biomechanics into clinical practice: current state and future prospects," *Curr. Eye Res.* **40**(1), 1–18 (2015).
- 195.G. Scarcelli, W. J. Polacheck, H. T. Nia, K. Patel, A. J. Grodzinsky, R. D. Kamm, and S. H. Yun, "Noncontact three-dimensional mapping of intracellular hydromechanical properties by Brillouin microscopy," *Nat. Methods* **12**(12), 1132–1134 (2015).
- 196.B. Heise, K. Wiesauer, E. Gotzinger, M. Pircher, C. K. Hitzenberger, R. Engelke, G. Ahrens, G. Grutznier, and D. Stifter, "Spatially resolved stress measurements in materials with polarisation-sensitive optical coherence tomography: Image acquisition and processing aspects," *Strain* **46**, 61–68 (2008).
- 197.D. C. Adams, L. P. Hariri, A. J. Miller, Y. Wang, J. L. Cho, M. Villiger, J. A. Holz, M. V. Szabari, D. L. Hamilos, R. Scott Harris, J. W. Griffith, B. E. Bouma, A. D. Luster, B. D. Medoff, and M. J. Suter, "Birefringence microscopy platform for assessing airway smooth muscle structure and function in vivo," *Sci. Transl. Med.* **8**, 359ra131 (2016).
- 198.T. Marvdashti, L. Duan, K. L. Lurie, G. T. Smith, and A. K. Ellerbee, "Quantitative measurements of strain and birefringence with common-path polarization-sensitive optical coherence tomography," *Opt. Lett.* **39**(19), 5507–5510 (2014).
- 199.S. K. Nadkarni, "Optical measurement of arterial mechanical properties: from atherosclerotic plaque initiation to rupture," *J. Biomed. Opt.* **18**(12), 121507 (2013).
- 200.G. Lamouche, B. F. Kennedy, K. M. Kennedy, C. E. Bisailon, A. Curatolo, G. Campbell, V. Pazos, and D. D. Sampson, "Review of tissue simulating phantoms with controllable optical, mechanical and structural properties for use in optical coherence tomography," *Biomed. Opt. Express* **3**(6), 1381–1398 (2012).

1. Overview of optical coherence elastography

The study and utilization of mechanics spans an enormous area of biology and medicine, ranging from the understanding of molecular machines and the production and sensing of forces and their effects on and in cells, to medical diagnosis of late-stage disease. Within the relevant range of length scales, from the molecular and sub-cellular to whole organs, there are not many techniques applicable in the sub-range spanning a single cell to aggregates of cells. One such technique suited to this sub-range is based on optical coherence tomography (OCT) and has come to be known as optical coherence elastography (OCE).

Elastography with OCT was proposed and demonstrated in the landmark paper published by Schmitt in 1998 [1], in which many of the principles and issues of contemporary research were laid out. Schmitt used OCT to image a sample undergoing bulk compression and assessed the resulting local displacement field by examining the correlation between cross-sectional (B-) scans of the same location. The results were used to produce elastograms, *i.e.*, cross-sectional maps of displacement, from which strain localized to a small region of the sample (*i.e.*, the local relative change in length per unit length) could be estimated.

Schmitt's work emphatically demonstrated that OCT could be used to gain information about a soft tissue's mechanical properties, and highlighted some of the opportunities and challenges that remain to this day. Firstly, mechanical image contrast is intrinsically different to optical contrast. To see an object in an OCT scan requires *differences* in scattering, produced by refractive index gradients, but mechanical contrast only requires sufficient scattering to obtain an OCT signal, and not that it varies in strength over the sample. Thus, inclusions invisible in OCT can be revealed by elastography [2], as shown in Fig. 1 [3]. Secondly, Schmitt measured local displacement and inferred strain, as shown in Fig. 2(a). Strain is a relative quantity related to an absolute quantity, an elastic modulus or Young's modulus, but, in most practical scenarios, in a complicated and not easily determined way.

Thirdly, viscoelasticity implies hysteresis in the dynamic mechanical response, which can be a source of information or image contrast, or a source of complication in attempting to measure elastic parameters.

Following Schmitt's seminal paper, six years followed before further papers were published, and although some progress was then made, the field remained embryonic, with only five groups publishing twelve papers in total until 2007. Only from around 2008 did the field experience an acceleration that has led to a plethora of groups working in the area today and the recent progress we report on here. In part, this progress has relied upon the evolution of OCT technology from the original time-domain systems to spectral-domain systems, which brought about two key advances: it enabled sub-envelope and sub-fringe axial displacements to be reliably detected by examining the interferometric optical phase, pushing into the sub-nanometer displacement regime; and it allowed the acquisition speed to be increased by several orders of magnitude, enabling the dual advantages of the reduced effects of extraneous motion and the acquisition of volumetric images.

The measurement of a relative mechanical property, such as strain (see Eq. (3)), may well prove to be sufficient in many applications, but in many other applications, it is expected that a quantitative reliable measure, such as an elastic modulus (Eq. (5)) – a ratio of stress to strain, will be required, spatially resolved with the OCT resolution or better. Measurement of this tensor quantity turns out to be complicated by the coupled nature of mechanical interactions, *i.e.*, by the fact that forces are readily transmitted across a sample and by the associated difficulty in measuring local stress. Even if the probing force (load) on a tissue could be applied only to a single voxel, which is generally not achievable, the connection of this voxel to all others means that the resulting displacement alone is insufficient to extract an accurate elastic modulus – combining such measurements with a computational model is required.

In this forward-looking review, we will seek to tease out these issues, highlight where progress has been made, and where work is still to be done. In so doing, we are cognizant of a number of recent reviews of the field [4–6], and will seek to advance upon these herein. Additionally, the reader is referred to more comprehensive descriptions of tissue mechanics [2] and of the field of elastography outside optics [7–9].

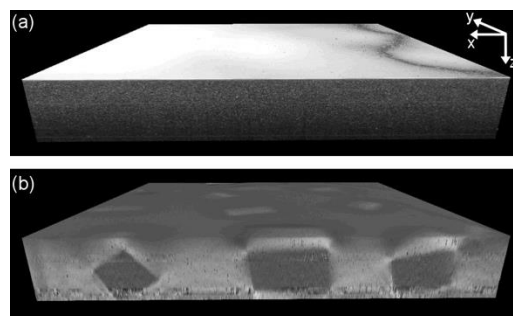


Fig. 1. (a) OCT and (b) OCE images of a phantom highlighting that optical and mechanical contrasts are not equivalent. Image sizes are 12 by 12 by 1.2 mm. Reproduced from [3].

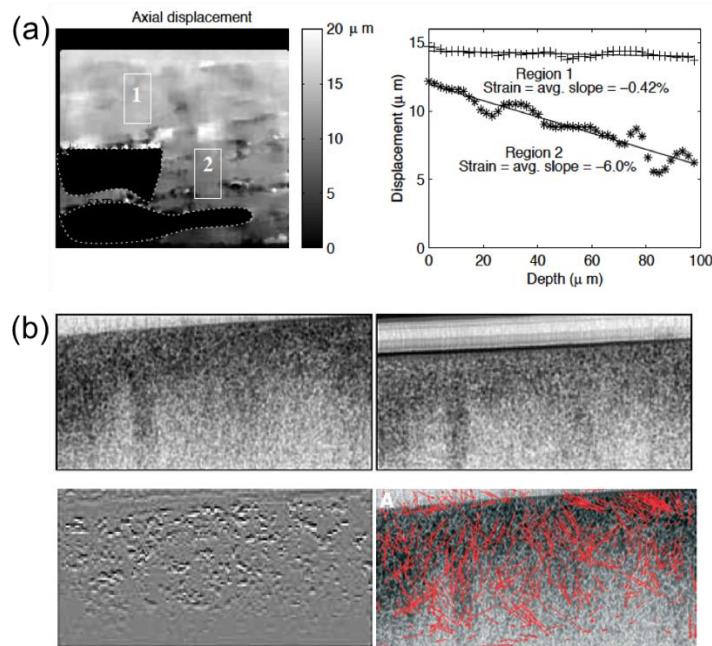


Fig. 2. Examples of early OCT elastography. (a) Axial displacement map of a pork meat sample (left). In dark regions, SNR is too low to evaluate. At right, average displacement versus depth for two regions marked in the map (right). Adapted from [1]. (b) Upper: OCT images before and after compression loading of an artery sample. Lower: Corresponding strain (left) and displacement maps (right). (21x21-pixel kernel. No scale provided.) Adapted from [12].

2. Optical coherence elastography prehistory

Here, we review the genesis of the field in order to provide a context for the remainder of the review. The term optical coherence elastography was first coined in a 2004 paper with Brett Bouma as last author [10] motivated by the then-emerging area of assessment of atherosclerotic plaque, which is now a major application of OCT [11]. Earlier that year, Rogowska *et al.* [12] had reported, in essence, a repeat of the Schmitt experiments, but now on *in vitro* aorta samples, successively loaded with weights, instead of using an actuator. The cross-sectional displacement maps, as shown in Fig. 2(b), did not show any recognizable structures, however, which did not suggest much promise. Later that year, Bouma and colleagues also began to explore the mechanical characterization of atherosclerotic plaque *in vivo* [10], an optical version of the then-emerging elastography based on intravascular ultrasound (IVUS) [13]. (We note in passing that the subsequent take-up of IVUS elastography has been slow [14]). They recognized that the effects of one or all of noise, non-rigid tissue deformation, and the breakdown of the assumption that speckle remained invariant under deformation, presented a great challenge to achieving robust arterial tissue velocimetry using light, indeed, difficulties that have still to be overcome in this application. They posed energy minimization as an alternative approach to tracking speckle (subsequently little used), investigated using finite-element analysis, and reported a single experiment on a laterally stretched aorta autopsy specimen, again showing modest promise. They also demonstrated the first use of OCT to provide reference image data (in place of histology) for biomechanical modelling of arteries [15], but this has not become widely used. In the following year, a subset of this group went on to consider how to address the inverse problem in extracting elastic parameters, and presented early results on simple inclusion targets based on simulated data [16], as well as inverse approaches to vascular elastography demonstrated on idealized

simulated data [17]. Others also followed similar approaches on synthetic arterial data [18]. We shall return to the important topic of inverse modelling in Section 6. Algorithms for optimizing speckle tracking remained a focus for the few researchers in the field into 2006 [19]. Of course, interest in speckle metrology, and in efficient algorithms for speckle tracking outside of OCE, goes back a long way [20], and was also an active field in the first half of the 2000s [19, 21, 22].

In 2006, Stephen Boppart's group first applied OCE to a tissue-engineered construct and to a developmental biology model – the *xenopus laevis* [23] (*xenopus laevis* has now largely been supplanted by the zebrafish and mice in developmental biology – a recent review of this field can be found in [24]). The basic method, compression, time-domain OCT and speckle tracking to determine cross-sectional displacement, had not changed since Schmitt's initial demonstration. The results, again, represented proof of principle.

These early reports were characterized by limited experimental data, a focus on speckle tracking and concomitant high loads leading to displacements (two-dimensional or uniaxial) of at least several 10s of [23], and sometimes in excess of 100, micrometers [12], exclusive use of time-domain OCT, and demonstration of proof of principle without being able to report compelling data. Most of the important technical issues in OCE based on compression of the whole sample were raised in these early papers in one way or another, but they failed to ignite the field, because the results presented did not approach the quality of images generated by OCT alone, as Fig. 2 emphasizes.

In the meantime, a revolution had been taking place in OCT, as described elsewhere in this Special Issue. Firstly, still using time-domain approaches, researchers had begun to capture the sub-envelope fringe information, initially to extract blood flow velocity from the Doppler-shifted fringe frequency [25, 26]. Secondly, starting from 2003, OCT began the move towards optical frequency-domain processing [27, 28], the so-called Fourier or spectral domain, employing a static interferometer, with either spectrometer-based detection of broadband illumination, or time-resolved detection of a swept-frequency optical source. Either method gave much easier access to the sub-fringe optical phase information than was available from optical delay scanners [29], which were intrinsically less stable. These methods also provided a gain in sensitivity approximately equal to the number of resolvable spectral channels, related to the reduction in shot noise per detection bin achieved without a reduction in overall signal [30–32]. Wang *et al.* were the first to put this to work in OCE, demonstrating milliradian equivalent nanoscale displacements (with averaging) in a tissue phantom via comparison of A-scans [33] and B-scans [34]. Although no tissue results were presented, this direction would prove to be pivotal over the next decade. There would be an explosion in the application of phase-sensitive methods, and in the range of elastography techniques to which they would be applied, as described in early reviews of this expansion [35, 36].

3. Methods overview

The field of mechanics uses many terms unfamiliar to optical scientists, and which even vary in their usage between sub-fields of mechanics. Here, we briefly attempt to cast some light on this, before defining terms more rigorously. Firstly, we point out the difference between material properties and stiffness. Although we often consider the intrinsic mechanical properties of soft tissue, as characterized by an elastic modulus, the overall mechanical behavior of a sample depends both on the material and the structure constructed from it. In general, the overall behavior is characterized by its stiffness, the ratio of force over resulting displacement. The elastic modulus, the underlying descriptive parameter, is generally defined as the ratio of applied tensile stress to the resulting strain. If in the linear regime, such that applied stress linearly affects strain in an isotropic material, then the elastic modulus is the Young's modulus (or the shear modulus), and tensile stress and compressive stress are identical. However, once beyond this regime (~few percent strain), then the applied stress

(including sign) at which the modulus is determined must be known. The modulus measured in this regime is the slope of the stress/strain curve, the tangent modulus, which is always greater than the Young's modulus. Finally, elasticity reflects the ability of an object to resume its shape after deformation – so, it is a general descriptive term that is related to what we measure, since the overall shape is not what we generally access.

So far, we have considered only a very small fraction of elastography methods; those based on quasi-static compression of the whole sample, because this method represents the genesis of the field, but there are a much wider group of methods that vary according to how the mechanical loading occurs, whether it is localized or global (relative to the volume being imaged), extrinsically applied or intrinsically present, and its temporal profile – quasi-static, harmonic or pulsed (transient), and whether elastic travelling or standing waves are generated and detected [8]. There are also a variety of ways in which the mechanical perturbations may be detected, providing a rich space to explore. Below, we outline basic definitions and assumptions within the framework of *static* (and quasi-static) and *dynamic* (harmonic and transient) OCE methods.

Static methods

The constitutive law for a linear isotropic homogeneous material in Cartesian coordinates (x_1, x_2, x_3) is described as:

$$\sigma_{ij} = \lambda \delta_{ij} \varepsilon_{kk} + 2\mu \varepsilon_{ij}, \quad (1)$$

where σ_{ij} is the stress tensor ($i, j = 1, 2, 3$), δ_{ij} is the Kronecker delta function (*i.e.*, δ_{ij} is 1 when $i = j$ and 0 otherwise), ε_{kk} is the strain tensor, ($i, j, k = 1, 2, 3$), and λ and μ are the Lamé constants with $\lambda = E\nu/[(1 + \nu)(1 - 2\nu)]$ and $\mu = E/[2(1 + \nu)]$ [2]. Here, E is Young's modulus and ν is Poisson's ratio. The relationship between the displacements u_i and u_j and strain ε_{ij} is:

$$\varepsilon_{ij} = \frac{1}{2} \left(\frac{\partial u_i}{\partial x_j} + \frac{\partial u_j}{\partial x_i} \right), \quad (2)$$

where u_i is the displacement in the x_i direction ($i, j = 1, 2, 3$). In the one-dimensional case, when an external force, F , is applied in one direction (for example, in the x_3 direction), these formulae can be simplified as:

$$\sigma = E\varepsilon, \text{ with } \varepsilon = \Delta L / L, \quad (3)$$

where σ , ε , ΔL , and L are the stress, strain, change in length, and initial sample length in the corresponding direction, respectively. The relationship between stress and force is given as:

$$\sigma = F / A, \quad (4)$$

where A is the cross-sectional area of the sample. Thus, inserting into Eq. (3), we obtain Young's modulus as:

$$E = \frac{FL}{\Delta LA}, \quad (5)$$

which readily applies to uniaxial compression and tension tests.

There are several complications in practice in applying this simple formula in quasi-static methods. Firstly, we wish to map the Young's modulus over a volume, and so wish to assess stress and strain locally. Strain is measured by assessing the local change in displacement per unit length, in one or more directions. The force (per unit area) distribution at the surface of a tissue can be measured with a stress sensor [37], but how this force propagates to produce local stress in the volume is not readily measured, presenting a problem for quantification. Finally, the stress-strain behavior of most tissues is highly nonlinear, meaning Young's

modulus is only accessed at very low values of strain, perhaps up to a few percent, and exceeds this at higher strains; but such responses vary greatly with tissue type. Thus, in general, the tangent modulus should be measured, the slope of the stress-strain curve, requiring strain (or stress) to be specified in order to be a reproducible quantity. These topics are explored further in Section 6.

Steady-state harmonic methods

If low-frequency excitation (typically in the sub-kHz range) is externally applied to a tissue, elastic waves of various types will be generated: longitudinal and shear waves in the volume, Lamb and Love waves in a thin layer, or Rayleigh waves on a surface [2]. The characteristics of this propagation can be used to reconstruct viscoelastic properties using an appropriate analytical model. If reflective boundaries exist, variations in regional elasticity can result in different vibration modes, which can also be used to deduce mechanical properties [38].

Some empirical viscoelastic models employ the one-dimensional form of Hooke's law based on the assumption that the tissue has a linear stress-strain relationship. Thus, a linear spring can be used to simulate the elastic material with the spring constant a measure of the sample stiffness [39]. In the Kelvin-Voigt model, for example, tissue is modelled as a parallel combination of a linear spring and a dashpot to, respectively, represent the elasticity and viscosity of the tissue. For an under-damped harmonic oscillator [40], the relationship between the loading force, $F(t)$, and the resulting displacement, $u(t)$, in the direction of the force can be written as a second-order differential equation:

$$m \frac{d^2 u}{dt^2} + R \frac{du}{dt} + ku = F, \quad (6)$$

where m is the mass of the sample, R is the coefficient of viscosity, and k is the spring constant. By solving this equation, one obtains the temporal displacement profile, $u(t)$, and the natural frequency, f , as:

$$u(t) = Be^{-\frac{R}{2m}t} \cos(2\pi ft + \varphi) \quad (7)$$

and

$$f = \frac{1}{2\pi} \sqrt{\left(\frac{k}{m} - \frac{R^2}{4m^2} \right)}, \quad (8)$$

where B is the displacement amplitude and φ is the phase. From Eq. (8), the stiffness of the sample, given by k , is linearly related to the square of the natural frequency, assuming a constant viscosity. If the viscosity can be neglected, the relationship between the spring constant and the natural frequency is simply $f = 2\sqrt{\pi m/k}$. For a fixed geometry, there exists a linear relationship between the resonant frequency and the square root of the Young's modulus [41]. When the external driving frequency matches the natural frequency, such resonances can be spatially and spectrally mapped as a source of mechanical contrast. Methods using non-resonant and resonant approaches are described in Sub-section 7.2.

Transient methods

Transient loading also leads to elastic wave propagation, which, in a homogeneous isotropic medium, is described more generally by [42–44]:

$$\rho \frac{\partial^2 \mathbf{u}}{\partial t^2} = (\lambda + \mu) \nabla \nabla \cdot \mathbf{u} + \mu \nabla^2 \mathbf{u} \quad (9)$$

where ρ is the material density, \mathbf{u} is the displacement vector, and λ and μ are the Lamé constants already defined. The displacement vector can be expressed in terms of a scalar potential φ_u and vector potential \mathbf{H}_u as follows:

$$\mathbf{u} = \nabla \varphi_u + \nabla \times \mathbf{H}_u. \quad (10)$$

Thus, Eq. (9) can be decoupled into compressional (longitudinal) and shear wave equations:

$$\frac{\partial \varphi_u}{\partial t} \nabla = c_p^2 \nabla^2 \varphi_u \text{ with } c_p = \sqrt{\frac{\lambda + 2\mu}{\rho}}, \text{ and } \frac{\partial \mathbf{H}_u}{\partial t^2} = c_s^2 \nabla^2 \mathbf{H}_u \text{ with } c_s = \sqrt{\frac{\mu}{\rho}}, \quad (11)$$

describing independently propagating waves in the bulk material, where c_p is the pressure (compressional) wave (P-wave) speed, and c_s is the shear wave (S-wave) speed. For soft tissues, the P-wave speed, typically several thousand m/s, is orders of magnitude faster than the shear wave speed, typically several m/s [2]. Because of the challenge of measuring such high speeds, and because the P-wave depends on the bulk modulus, which varies little between soft tissues, P-waves have been less studied to date. The shear wave speed, c_s , can be used to estimate Young's modulus (neglecting viscosity) from:

$$E = 2\rho(1+\nu)c_s^2. \quad (12)$$

The elastic wave propagating near the surface will, in general, comprise both surface longitudinal and vertical shear components – the Rayleigh wave. The surface wave speed, c_R , can also be used to estimate E (again, neglecting viscosity) as

$$E = \frac{2\rho(1+\nu)}{\left(\frac{0.87+1.12\nu}{1+\nu}\right)^2} c_R^2. \quad (13)$$

Due to the high content of water, tissues may generally be assumed to be incompressible, so Poisson's ratio can be reasonably assumed $\nu \cong 0.5$ [8] and, thus, Eq. (12) can be further simplified as: $E = 3\rho c_s^2$, and $c_R = 0.953c_s$.

From these expressions, we can see that the shear wave speed ideally relies on the material properties alone. In practice, boundary conditions, viscosity and variations in excitation frequency can all drastically affect wave propagation, invalidating these simple expressions [45]. Thus, development of appropriate analytical models is necessary to accurately quantify tissue biomechanical properties, as will be extensively discussed in Section 7.

4. Displacement measurement

Having broadly described the nature of the displacement taking place in samples, in this section, we briefly introduce the two main methods used to measure it, speckle tracking and phase-sensitive detection, before describing in Sections 6 and 7 how these methods are applied in the context of particular OCE methods.

Speckle tracking was the means of measuring displacement in early OCE studies [1,4], accomplished via variants of digital image correlation (DIC), itself, a much larger field [21, 22]. Typically, vectorial displacement is determined from cross-correlation of a multi-pixel kernel between cross-sectional images from the same or close-by location. This process necessarily degrades the spatial resolution of the elastogram, but the sensitivity of the displacement measurement, by contrast, can be improved to below the pixel size by interpolation [46]. In cross-sectional images, out-of-plane deformation artifacts may occur, which can be avoided with digital volume correlation speckle tracking described in Section 6.

A key limiting factor on speckle tracking arises because of its origins in coherent wave superposition. Beyond displacements equal to a small fraction of the OCT speckle size, decorrelation rapidly occurs as the object is deformed [47]. These factors are considered in detail in Section 6.

The other main method, phase-sensitive detection, utilizes the phase of the complex OCT signal, rather than the structural information obtained solely from the intensity. Phase-sensitive methods, made practical by the emergence of Fourier-domain OCT (see end of Section 2), take the displacement sensitivity to sub-nanometer levels [48], enabling ultra-sensitive detection of deformation [33, 34, 49]. Such methods have become predominant in OCE. However, they achieve this high sensitivity, as noted, in a single axial dimension.

There are various sources of phase noise that impair phase-sensitive detection. In the high signal-to-noise ratio (*i.e.*, the shot-noise) limit, the minimum phase *difference* that can be measured (twice that of a single phase measurement) is given by $1/\sqrt{SNR}$ [50], and this expression has been shown to hold in practice over the range of typical OCT SNRs, from 20 to 45 dB [50]. Thus, if we set a practical upper limit in tissue on OCT SNR of, say, 50 dB, the minimum detectable phase difference is 3 mrad, and the change in axial displacement, Δu_z , given by $\Delta u_z = \Delta \phi \lambda / 4\pi n$, for wavelength, λ , of 1300 nm, and refractive index, n , of 1.4, corresponds to 0.23 nm, without averaging. At a more typical SNR of 20 dB, this becomes 7.4 nm. There are many technical sources of phase noise, such as frequency jitter in a swept-wavelength source, environmentally induced differential phase shifts in the interferometer, and undesired sample motion. Noise from frequency jitter in the source can be overcome with optical frequency referencing techniques, such as the use of a fiber Bragg grating [51] or Mach-Zehnder interferometer to perform spectral recalibration or more precise triggering. Environmental noise can be reduced by utilizing a common-path interferometer [52]. For sub-surface axial strain measurement, use of linear fitting over a region improves the accuracy and robustness of compression-based strain estimation [53, 54].

Phase-sensitive detection also suffers from the ambiguity caused by phase wrapping. Unwrapping the phase is possible, but sensitive to noise. In compression OCE, by spatially averaging and weighting the displacements based on the SNR, up to 5 cycles have been unwrapped and shown to provide a more robust estimate of the strain gradient [52, 55]. The upper limit on phase unwrapping is set by speckle decorrelation [47]. Alteration of the underlying amplitude and phase of the speckle pattern means the phase can no longer be tracked and unwrapped accurately, in essence, manifesting the same issue as for speckle tracking.

Phase-sensitive methods can be improved by motion artifact compensation algorithms [56]. Furthermore, for depth-resolved imaging of elastic waves in multilayered tissues, where each layer has distinct optical and mechanical properties, correctly accounting for refractive index mismatches is necessary [56, 57]. The measured unwrapped temporal phase profile at a given depth from within a homogeneous sample, $\phi_{in}(t)$, is converted to displacement, $u_{in}(t)$, after correcting for the sample surface motion and refractive index mismatch between the sample and external medium (such as air or water) [57] as:

$$u_{in}(t) = \frac{\lambda_0}{4\pi n_{sample}} \times \left[\phi_{in}(t) + \phi_{surface}(t) \times \frac{n_{sample} - n_{ext}}{n_{ext}} \right]. \quad (14)$$

Here, λ_0 is the central wavelength of the OCT source, n_{sample} and n_{ext} are the refractive index of the sample and external medium, respectively. Consequently, phase-sensitive analysis of propagation through multiple, distinct layers should account for each layer by increasing, as necessary, the number of terms in Eq. (14).

There remains considerable scope for improvement of displacement measurement methods. One recent approach utilizes both intensity-based correlation techniques and phase-sensitive techniques to track displacements in cross-sectional images, achieving a displacement sensitivity of $0.3\ \mu\text{m}$ [58, 59]. A related method was also proposed to increase the dynamic range of the axial displacement measurements [60]. Doppler variance techniques may also provide a pathway to more robust phase-sensitive measurements [61, 62]. Better displacement sensitivity will benefit many instances, *e.g.*, for dispersion measurements of an elastic wave [45, 63], or as input to analytical models of the tissue temporal response [64].

5. Loading methods

In Section 3, we briefly described methods of probing mechanical properties through the presence of displacement fields in the tissue. In Section 4, we briefly described how the displacement can then be measured. Here, we describe how the displacements are induced in the first place. The choice of loading method is generally dictated by requirements of the application. Loading methods can be broadly classified as contact or noncontact, extrinsic or intrinsic, localized or global (relative to the volume being imaged), and static or dynamic. We now describe in some detail the wide range of specific implementations shown in Fig. 3.

The first demonstration of OCE by Schmitt utilized static, global, planar compression induced by an annular piezoelectric actuator and window, applied from the same side of the tissue as used for imaging [1]. Such static, full-field compression was the only method used until 2008. Application of uniform stress across the sample is key to generating comparable displacements at all points across the field of view, and key to simple interpretation of the elastograms [4]. In the case of a curved sample, such as the eye, a curved gonioscopy lens has been used to address this issue [65–68]. This issue also applies to loading lumens, such as arteries. Local contact (indentation) loading has been little used in the static context [69] but more so in the dynamic context as a point source of elastic waves [70–72]. Local quasi-static indentation utilizing a needle containing a built-in forward-looking OCT probe (A-scan only) has been demonstrated to enable tissue characterization at depths well beyond the maximum OCT penetration depth of a few millimeters in tissue [69, 73]. Indentation using an atomic force microscope cantilever tip takes the issue of localization of load to its extreme, but the lateral OCE resolution remains limited by the optical system [74].

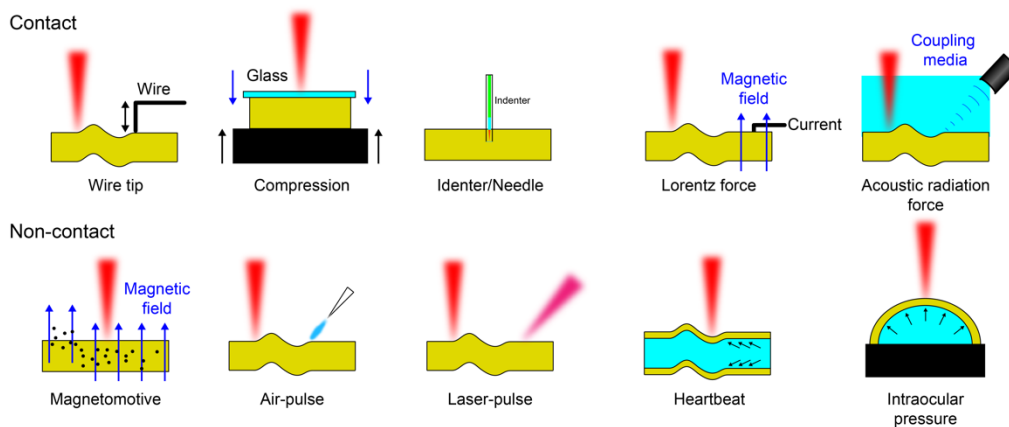


Fig. 3. Typical loading methods.

Quasi-static global compression has been demonstrated in several scenarios, including non-contact: using an impulse air jet for average measurements of mechanical properties [75] and for imaging the effects of an air puff on corneal deformation [76, 77]; and contact: for imaging of continuous acoustic frequency loading [78]; in both the latter cases avoiding the

propagation effects of any waves generated on or in the tissue. Alternatively, global standing wave generation has exploited the mechanical resonance of the cornea through non-contact acoustic excitation at audio frequencies and detection of vibration modes by OCT [79, 80]. Non-contact point excitation of a wave on the cornea, using a micro-jet air puff, has subsequently been demonstrated extensively, as described further in Section 7 [81].

Non-contact loading through use of sound at frequencies above the acoustic range rapidly becomes problematic, due to the high attenuation of ultrasound in air, the high impedance mismatch between air and tissue, and the challenge of directly measuring the resulting tissue response in the megahertz range [8]. It is important to firstly realize that ultrasound-based loading, to date, has almost exclusively been a contact method. Secondly, the use of ultrasound loading has taken advantage of the so-called acoustic radiation force (ARF), adopted from ultrasound elastography [82]. ARF in OCE makes use of 10s μ s–10 ms bursts of ultrasound in the megahertz range to modulate the force applied to the sample. The resulting displacement has been detected as the axial displacement along the ultrasound beam at focus [83–87] or as an axial displacement associated with a shear wave generated by the burst at some lateral offset from the focus [88–90]. By scanning the frequency of the amplitude modulation, it has also been demonstrated that acoustic mechanical resonance can be detected along the axial direction [91]. Shear wave propagation can be characterized in the orthogonal geometry, *i.e.*, with the ultrasound beam orthogonal to the OCT beam [62], a somewhat limiting geometry for general applications, but suited to some [92]. ARF can apply localized tissue displacements in the micrometer range at depths well beneath the surface of the tissue. Whilst this localization is effectively point-wise loading for ultrasound elastography, it is more extended in the case of optics. For example, in [88], the depth of field of the ultrasound signal was ~ 3 mm and the full-width at half-maximum beam width was ~ 0.25 mm, an order of magnitude larger than the OCT resolution; and in [93], the ultrasound beam was assumed uniform over a 0.3×0.5 mm lateral region. Another potential benefit of ARF is that it could be integrated into catheter-based probes, as demonstrated at 10 mm diameter in [85]. With further miniaturization, such catheters may enable intravascular mechanical assessment of the arterial wall, a long-held goal, producing in a catheter the types of measurements currently only possible *ex vivo* [89, 93]. ARF produces sufficiently large pressures to be of safety concern for applications in the eye [94]. Investigators led by Wang and O'Donnell adopted a chirped-pulse radar method to reduce the peak ARF. Lower pressure frequency-chirped long-pulse ultrasound induced shear waves [94] were numerically compressed post-detection into a short, localized high-pressure pulse. Most recently, technological innovations in piezo-ceramic materials from the same group have enabled the realization of high-power ultrasound transducers capable of air-coupled ARF excitation [95]. Such transducers, recently demonstrated for OCE in *ex vivo* porcine cornea [96], present intriguing possibilities for non-contact OCE.

Point dynamic loading is attractive as a source of shear waves, and an attractive *non-contact* localized method is the micro-air puff developed and applied extensively by the Larin group [45, 57, 63, 81, 97–116], mainly to the cornea, but also to skin [108, 116], cardiac and skeletal muscles [104], cartilage [101, 106], fat and soft tissue tumors [97], and kidneys [112]. Similar to ARF-based excitation, an air puff can deliver a localized and well-controlled impulse stimulus, which can be accompanied by measurement of the tissue displacement or measurement of the air puff-induced elastic wave. A major benefit of the air puff is the possibility of using very small loading pressures (in the mPa range). At the same time, this method is limited in how short the impulse can be – a minimum of ~ 0.8 ms has been demonstrated [81], which restricts the bandwidth of the elastic waves available for quantifying tissue viscoelasticity (extensively discussed in Sub-section 7.1). Additionally, in contrast to ARF, it is limited to surface excitation, and cannot excite the sample internally, except through the surface.

An attractive all-optical excitation method using pulsed laser-induced photothermal waves was demonstrated by Li *et al.* [117, 118]. Similar to the air puff, the pulsed laser is truly non-contact, and preferentially excites from the surface, but with some sub-surface penetration, depending on beam design and tissue properties. Recent studies have demonstrated the use of laser-induced elastic waves to characterize the elastic properties of the urinary bladder [119] and skin [120]. One of the benefits of this method is the shared optical path for both excitation and imaging components, which could result in very compact optical probes. Whilst ultra-fast OCE techniques can capture the wave without repeated excitations [107, 121], there remain safety concerns over optical fluence levels necessary to overcome the limited capability of tissues to absorb laser energy and the resulting low displacement amplitudes. These same concerns apply to the field of photoacoustic tomography, which is based on contact acoustic detection of the same waves [122], and has begun to see exploration of elastography [123].

There are several other interesting loading methods to consider before concluding this section. Most recently, elastic waves were induced by the Lorentz force generated when electrical current induced by an external alternating-current magnetic field flows through the sample [124]. Since biological tissues are inherently conductive, this method makes possible a wide range of investigations using biocurrent and tissue conductivity to study not only biomechanical properties, but also electrophysiological properties. A related alternative, extensively investigated by the Boppart group, is the use of magnetic nanoparticles, incorporated into tissues placed in an external magnetic field, as internal transducers for magnetomotive vibration [125–139]. Thus, loading is highly localized, to individual or aggregations of nanoparticles, but distributed throughout the tissue, and dynamic, in the alternating-current magnetic field. Nanoparticles can be functionalized to selectively target tissues of interest [127, 136, 138]. The particles can be used to induce elastic waves [133] or spectroscopic analysis can be performed by sweeping the excitation frequency and finding resonance modes for micro-rheological analysis [125, 131]. To date, there has been limited uptake of this method by other groups [129], perhaps because of the challenges presented by the very small displacements that can be induced. Measurable displacements throughout the tissue requires a sufficiently high magnetic field gradient and relatively high concentrations of nanoparticles to achieve a sufficient OCT signal. Thus, for *in vivo* applications, a challenge is to maintain sufficiently low toxicity.

A genuinely exciting alternative to external loading is to utilize body motion as an intrinsic loading source. In all cases, the idea is to measure tissue displacements caused by the body itself, thereby, avoiding the need to introduce a load. An excellent example of this is in the companion field to OCE of Brillouin microscopy [140], in which the Brillouin frequency shift caused by thermally generated acoustic phonons describes mechanical properties (longitudinal modulus) on the micrometer scale. In this method, hyperspectral Brillouin micro-spectroscopy is conducted in a confocal microscopy geometry using a monochromatic laser source. On the opposite extreme of length scale, pulsatile blood flow produces pulse waves propagating along blood vessels, and their speeds and patterns have been related to average arterial stiffness [141, 142]. Vessel pulsatility has been used in OCE to quantify stiffness of arteries in developing chick embryos, by imaging from outside the vessel [143]. Pulsatile motion has also been utilized in other tissues and forms of elastography, such as the thyroid with ultrasound elastography [144] or the brain with magnetic resonance elastography [145], including a curious example in which head shaking was used as the source of elastic waves [146]. Even changes in the intraocular pressure, which generate corneal displacements, have been used as a loading source [147]. Such “internal” methods, utilizing voluntary or involuntary body motion as a source of elastic waves or tissue displacement that may be characterized by OCT, are definitely worthy of further attention.

6. Static methods and applications

6.1 General considerations

Static methods, or quasi-static methods as they are often called because they involve some dynamics, must intrinsically *avoid* the complications of the generation of waves. Methods *exploiting* the generation of waves will be discussed in Section 7. As discussed in Section 5, static loading may be point-like, or cover any area of the sample surface. Simultaneously applying a uniaxial and nearly uniform level of stress to the whole field of view to be imaged, with a single actuation and device, is an efficient and ideal loading method. Whilst this can, in principle, maximally exploit the speed of an imaging system, since the whole volume undergoes displacement, it also brings with it the complication that strain in a given voxel does not depend solely on the mechanical properties of that voxel. The applied stress, in effect, propagates through the sample in a way that depends on the mechanical properties of the surrounds. Thus, displacement, and any local strain derived from it, will be largely representative of local mechanical properties – and generate mechanical contrast, but stress will remain unknown, unless the sample is of very simple geometry, such as a set of homogenous layers [148]. Thus, extracting a property, such as an elastic modulus, from OCE based on global, compressive loading is a challenge which must invariably involve computation [8], further discussed in Sub-section 6.5

To complicate matters further, the mechanical response to a load is not solely instantaneous because soft tissues are *viscoelastic*. Dealing with this issue can involve merely waiting for transients to decay (for up to several minutes [149]!), or attempting to exploit the time dependence to extract more information. However, such studies of *viscoelasticity* in OCE are in their infancy [45, 109, 110, 150]. At the same time, as described in Section 3, soft tissue responds in a nonlinear fashion to stress and the tangent modulus depends on stress, or equivalently, strain. The study of how stress affects mechanical contrast, and the reporting of strain when reporting an elastic modulus, has not yet commenced, and is an area of future opportunity. However, we should not anticipate too much too quickly, as similar issues continue to afflict ultrasound elastography, which has a much longer history than OCE [8]. In Sub-sections 6.2-6.4, we describe quasi-static strain imaging via compressive elastography, before going on to consider how such methods may produce a measure of the elastic modulus.

6.2 Quasi-static compression and the example of breast cancer

Like so much of Schmitt's work, his pioneering paper on OCE was well ahead of its time in concept and realization. Schmitt's images were superior to most subsequent published work until about 2014, when a group led by one of us demonstrated much more compelling images of soft tissue contrast [52], a recent example of which is shown in Fig. 4 [151]. Why did this advance take so long? In essence, it required the maturation of a number of aspects of the technology: 1) sufficient acquisition rates with Fourier-domain OCT to make volumetric imaging routinely possible, in turn, making *en face* axial strain imaging feasible; and 2) phase-sensitive detection with sufficiently low technical phase noise and robust signal processing methodologies [52, 53] to provide displacement sensitivity in the sub-nanometer range, extending over a few-micrometer range. The other key element required to move the field forwards was the development of the technical capacity to match OCT and OCE cross-sectional images with closely corresponding histology, and not merely representative or nearby histology, thereby enabling interpretation by a pathologist [152]. This element is, indeed, required in nearly all applications of OCT and has been slow in coming.

Whilst quasi-static compression elastography has been demonstrated in various tissues [153, 154], elastography of breast cancer represents a great challenge, because breast tissue is highly mechanically and optically heterogeneous, involving very soft, largely transparent and membranous adipose, optically dense stiffer benign stroma and a wide range of tumor types, but additionally, fluid-filled vessels and a network of ducts (which in *ex vivo* scenarios are, in

essence, empty tubes) terminated in lobules. Further, when such tissues are excised, the cut surface tends, through mechanical relaxation, to take on a topography reflecting, to some extent, the internal heterogeneity, further complicating the application of uniform, uniaxial stress. Thus, such images can show strain of both signs: compressive (usually negative values) and tensile (positive values), as described in [155]. Such relative contrast cannot be readily mapped to the underlying tissue elasticity in any quantitative sense and, as a relative measure, it cannot be compared to other samples. All of this might seem to be a major problem, but the extent to which it really is a problem is entirely dependent upon the application. In the case of breast cancer lumpectomies, the goal is to assess the margins of the sample for the presence of tumor to guide the surgery, with the goal of reducing the high rates (20-40%) of re-excision currently experienced [156, 157]. Evidence accumulated from more than 58 specimens [52, 151, 155] shows strong correlation between tumor or benign stroma diagnosed in histology and the texture of the *en face* strain elastograms. Distinguishing between benign and malignant solid tissue has been a challenge faced by OCT at conventional resolutions (5-15 μm) [158]. Whereas adipose and solid tissue can be readily distinguished by OCT alone, distinguishing between solid tissue types has been problematic, with scattering contrast alone proving inadequate for providing the necessary surety in most scenarios. Adding mechanical contrast to the scattering contrast shows the promise of resolving this issue, whilst employing conventional OCT resolution. Finally, on the topic of breast cancer, other groups have examined breast tissues using a variety of methods [159]: strain-based [160] and dynamic OCE [41], high-resolution OCT and its variants [161, 162], *in vivo* probe-based OCT in the excision cavity [163], photoacoustic tomography methods [164] and Raman spectroscopy of nanoparticle contrast agents [165]. It is not yet clear which method will prove best, but beyond accurate assessment of involved tissue, the application to margin assessment will require ready assessment by the surgeon of all relevant tissue in less than 30 min in total, and will likely favor an intra-cavity solution [163].

6.3 Speckle tracking in quasi-static compression

In the meantime, other groups have been seeking to advance compression methods based on speckle tracking [46, 149, 166, 167], largely borrowing from digital image correlation [21, 22] methodologies, as described in Section 2. Such methods have also been developed for volumes, so-called digital volume correlation, which was first developed for X-ray computed tomography [168]. (As an aside, “speckle” in image correlation is sometimes not the coherent speckle we observe in OCT, but often describes the effect of imaging artificial texture applied to a sample surface [167, 169].) Digital volume correlation methods have recently been applied to OCT [149, 166], enabling measurement of the full strain tensor. Speckle tracking methods require the speckle field in both images to remain correlated, thus, displacement between measurements must be limited to around half of the speckle size [47, 166], commonly corresponding to strain in the 1-2 percent range. Then, correlation averaging kernels (volumes here) must contain sufficient speckles to enable sufficiently accurate displacement measurement, representing a trade-off between spatial resolution and strain sensitivity and degrading the resolution of the measurement compared to the underlying OCT resolution. Kernel size has varied widely in the speckle-tracking literature to date, from 7 to 16 pixels [1], to a few voxels [149], to many tens of voxels [166]. This resolution degradation is to be contrasted with phase-sensitive, compressive OCE, in which the lateral resolution of OCT is maintained, but only the axial strain component is measured, and with axial resolution that is close to that of speckle tracking [4]. Figure 5 shows a selection of OCE images obtained using compression and speckle tracking.

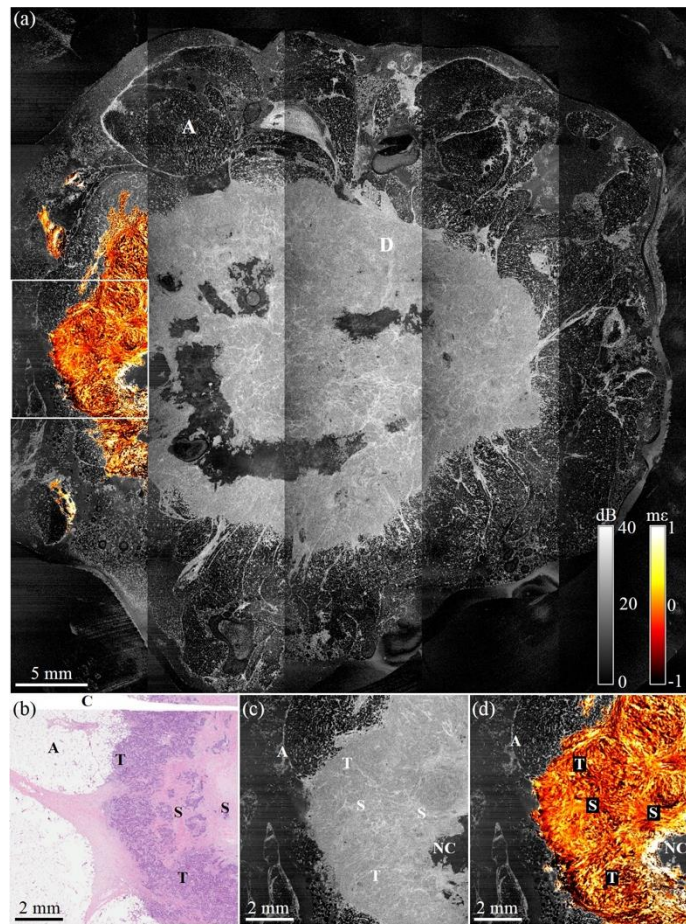


Fig. 4. Wide-field compression micro-elastography (OCME) of a freshly excised malignant tumor. (a) Wide-field *en face* OCME overlay on OCT stitched image of the entire sample, measuring 47.5×47.5 mm. (b) Histology, co-registered with OCT and OCME. (c) *En face* OCT image showing a $1.6\times$ magnification of the boxed region in (a). (d) Corresponding *en face* OCME overlay. A, adipose; C, cassette stitching artifact; D, dense tissue; NC, non-contact; S, stroma; and T, tumor. Reproduced from [151].

6.4 The opportunity of higher resolution elastography

In general, moving to higher resolution measurements brings with it the benefit of resolving cellular scale structures that are observed in histology, whilst suffering a reduction in the field of view. Early indications are that in applications such as breast cancer, the capacity to resolve such micro-structures addresses, at least to some degree, the issue of differentiating benign from malignant tissues [161, 162]. In moving to higher resolution, OCE faces an additional challenge in that, since the speckle decorrelation length scales with speckle size [47, 166], this reduces the maximum displacement that can be measured between frames. This issue can always be addressed by collecting more frames per measurement, incrementing the displacement by less per frame, so as to maintain correlation, but this adds to the acquisition overhead. Nonetheless, several recent studies have shown promise in this regard [149, 170, 171], demonstrating substantial improvements in resolution, as shown in Fig. 6. Such resolutions suggest the capacity to assess mechanical properties of cells and several preliminary studies have been reported [170, 172]. Cell mechanics is a complex and crowded field, with its own suite of techniques [173], including traction force microscopy, pipette microaspiration and atomic force microscopy, amongst others, and is often concerned with

measuring forces on or applied by cells, rather than their mechanical properties. It remains to be seen how OCE will impact this field – the naïve expectation is that it should be able to characterize cell aggregates or even thick tissue sections, which is rather hard to do now. However, this suggests penetration depths of several hundred microns, whilst maintaining sub-cellular scale resolution, which, notwithstanding the promise shown in [171], has not yet been convincingly achieved.

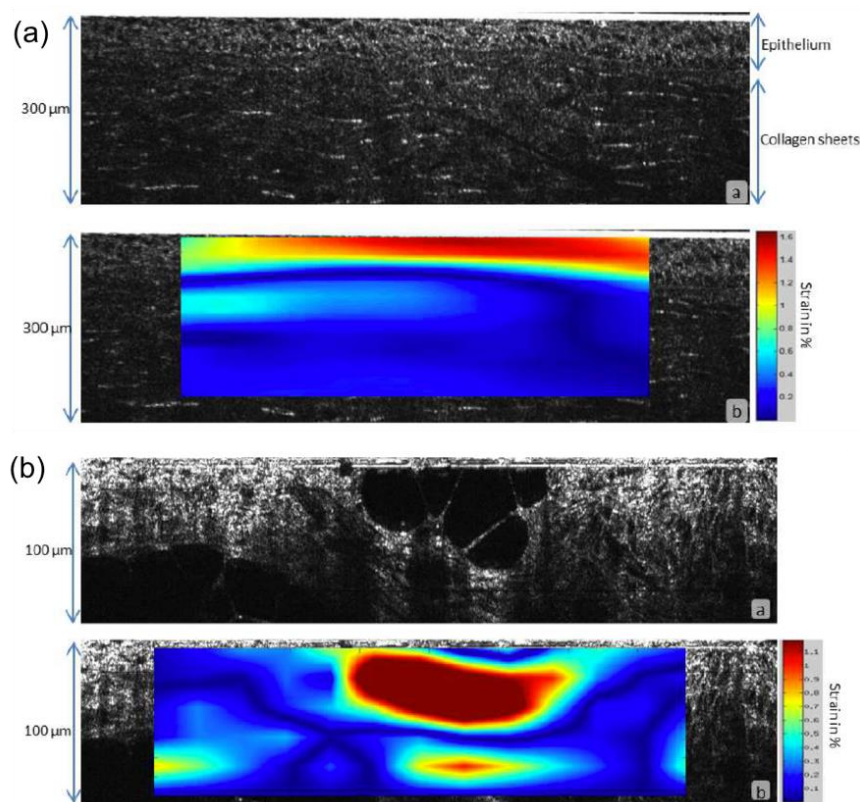


Fig. 5. Examples of quasi-static compression OCE using full-field, ultra-high-resolution OCT and digital volume correlation processing: in each figure part, OCT (upper) and overlaid strain map (lower). (a) cornea; (b) breast tissue. Adapted from [149].

6.5 Beyond the imaging of strain – towards quantitative compression elastography

Moving beyond the relative measure, strain, to a quantitative measure, such as an elastic modulus, is complicated, as described in the opening paragraph of this section. Not only is stress at a given voxel generally not known and influenced by such variables as surface topography, friction and elastic properties outside of the imaging field of view, but the measured modulus can also depend on frequency (even in the quasi-static regime) [174]. Possibly because of these complications, the overall availability of reference data on soft tissue properties is limited [8]. Nonetheless, the attraction of being able to compare different samples, and to monitor the same sample over time means that it is attractive to pursue quantitative methods, which will be further exemplified in Section 7.

Many early works have combined measured displacement fields or strain fields with a model to extract a parameter, or even one step further back, have merely used the structural image as a starting point for a mechanical model [15, 17, 175]. The next step along this path is to use compressive OCE data to determine average values of the elastic modulus, which has been done using quasi-static compression on human arterial tissue [176] and, dynamically,

using a Kelvin-Voigt model on various phantoms and tissues [41, 83]. There have also been several early papers on developing sophisticated models based on fully synthetic input data [16]. However, most models suffer from too many degrees of freedom unless they can begin with, at least, the full measured displacement field and, ideally, knowledge of the load and boundary conditions. An approach to converting experimental displacement data to elastic modulus was recently advanced by Fu *et al.* [166], who combined volumetric vectorial strain obtained from digital volume correlation with a virtual fields model, which is based on the principle of virtual work. The output of the model is still only a single average Young's modulus of the sample.

Recently, a novel approach was put forward to enable the assessment of surface stress whilst determining volume axial strain [54]. By imaging through a transparent compliant layer, for which the stress/strain behavior is well characterized, it is possible to use the OCT data to measure strain in the layer, thereby, inferring axial stress at the sample surface. This measurement can be used to calibrate the volume axial strain to provide an elastic modulus that is accurate under the assumption that stress does not vary with depth, which is true if the only mechanical heterogeneity is in the axial direction [148]. This is already a considerable advance on previous methods allowing one to overcome the so-called soft/stiff problem [37], in which a stiff area of the sample shields a soft area from strain, making it appear stiffer than it actually is. It can also be used in stand-alone form to mechanically 'palpate' tissues thereby being sensitive to all depths in a tissue, not just the region accessible to OCT [37, 177]. In all cases involving use of a continuous compliant layer, there is some sacrifice of lateral resolution in the measurement caused by the layer's mechanical continuity.

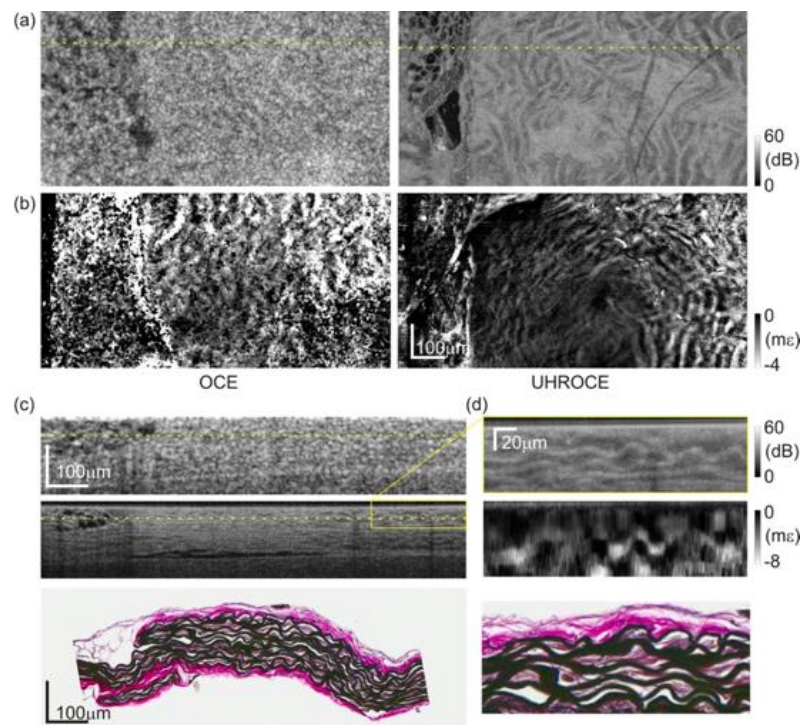


Fig. 6. OCT images and strain elastograms of a mouse aorta taken with standard and ultra-high resolution systems: OCE and UHROCE. (a) *en-face* OCT images within the *tunica media*. (b) Corresponding *en-face* strain elastograms. (c) OCT B-scan images of the aorta cross-section (taken with OCE – top – and UHROCE – middle), and histology (bottom panel) from corresponding but not identical section. (d) Speckle-averaged magnified portion (top inset) of the structural B-scan image in (c), corresponding B-scan strain elastogram (middle inset), and representative histology (bottom inset). Reproduced from [171].

Whether or not a layer is being used, the issue of accounting for friction between the loading plate and the sample must be carefully considered in seeking to evaluate the modulus [148]. This issue is further compounded when using a layer, because it, too, is subject to friction-induced artifact, altering the apparent surface stress. Such artifacts remain a barrier to quantitative comparison, but can be accounted for, in principle, by a computational model, if the friction can be estimated.

Very recently, a group involving one of us has attempted to use this surface stress data, in combination with cross-sectional displacement data, as inputs into an iterative inverse finite element model, with interesting first results [178]. A weakness of such iterative methods remains their sensitivity to the setting of the so-called regularization parameter, in the presence of too many degrees of freedom. In a volume model, which is, indeed, computationally feasible, this feature can be tightened by more input data, such as volumetric axial displacement in the tissue and in the compliant layer – which is a very promising prospect.

7. Dynamic methods and applications

Dynamic OCE techniques mainly utilize phase-sensitive detection of elastic wave propagation to be considered in Sub-section 7.1. The term dynamic OCE also applies to related dynamic loading and detection methods, which, rather than assessing propagation, analyze steady state deformation, which we consider separately in Sub-section 7.2.

7.1 Surface elastic wave methods and applications

Since the OCT imaging depth is limited to the first few millimeters in a turbid tissue, analysis of elastic waves is largely limited to surface layers. Most transient loading methods described in Section 5 generate a point-like axial longitudinal displacement which launches a shear wave. Such waves propagating near the surface (Rayleigh waves) comprise both longitudinal and vertical shear components, relative to the direction of travel. Rayleigh waves travel at slightly lower speeds than pure shear waves (see Eqs. (12)-(13)), with an amplitude that decays exponentially with depth into the tissue. When guided in layers (such as in the cornea), they are referred to as Lamb waves, or Rayleigh-Lamb waves.

Analysis of surface elastic wave propagation can be divided into temporal and spatial approaches, as shown in Fig. 7. Temporal approaches involve analysis of the transient displacement at one position as function of time by quantifying parameters such as displacement amplitude, recovery rate, and frequency dependence. Spatial approaches involve analysis of propagating elastic waves as a function of position by quantifying parameters such as amplitude decay, and group and phase velocities and their frequency dependence. All of these methods (and their combinations) provide information on viscoelastic properties via appropriate analytical models, as we describe in detail in the following.

Spatial assessment of elastic wave propagation has been extensively utilized in both ultrasound elastography [82] and magnetic resonance elastography [179], and many of these methods have been adopted in OCE. The elastic wave velocity can be calculated from the ratio of the propagation distance to the time delay, which is usually obtained through the cross-correlation of the OCE-measured local axial displacement profiles along the wave propagation path (see Fig. 8(g)) [104, 180]. As indicated by Eq. (12), under ideal conditions, there is a simple and direct relationship between shear wave speed and Young's modulus. Thus, measuring the wave speed at different spatial (in-depth and/or lateral) locations allows mapping and quick *estimation* of elasticity, as shown in Fig. 8. However, Eq. (12) is derived under several important assumptions about the sample, such as neglecting viscosity, which we consider further below [181].

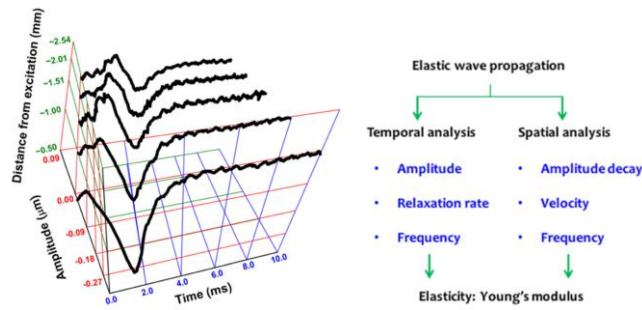


Fig. 7. Principles of analysis of elastic wave propagation originating from a point source.

To calculate the wave speed, in principle, measurements from only two spatial locations are required. In practice, to obtain reliable elastic wave velocities, measurements from 20 to 30 spatial locations are used, such as shown in Fig. 8(g), reducing the spatial resolution achieved as a consequence. To see this, consider that the elastic wave velocities in most soft tissues range from 1 to 5 m/s. The transit time for a wave travelling at 5 m/s to travel 3 mm is ~ 0.6 ms. To image the propagation with 100 μm transverse spatial resolution, requiring 30 frames across the imaged region, requires an OCT B-scan frame rate of 50 kHz. In order to maintain the same lateral resolution in the B-mode image (100 μm), an A-scan rate of 1.5 MHz is required. Recent technological innovations in Fourier-domain mode-locked (FDML) laser technology have allowed such high frame rates to be achieved, and ultra-fast OCE of the cornea has been demonstrated by two groups, including one of us [107, 121]. This method, in which multiple successive B-scans are acquired from a single mechanical impulse, features acquisition times of less than 10 ms, the fastest demonstrated to date. However, this ultra-fast OCE technique implies an inherent trade-off between the temporal and transverse spatial resolutions. Whilst the transverse spatial resolution can be increased to 10s of μm via post-processing of multiple temporal scans acquired at different spatial locations with multiple mechanical stimulations [103, 180], it intrinsically increases the acquisition time to several seconds or longer. Improving both the temporal and the transverse spatial resolutions are absolutely required in future clinically oriented OCE developments, which is a fast evolving area of research [182–185]. We note in passing that axial (depth) resolution of shear wave-based OCE methods is limited, in theory, to the OCT axial resolution (typically on the order of 7–15 μm), but the practical limits have yet to be comprehensively investigated.

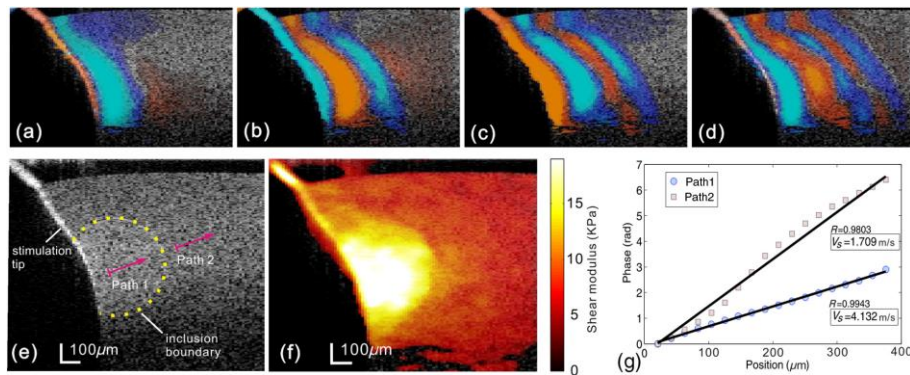


Fig. 8. (a-d) Displacement field B-frame images at 2 ms intervals recorded from an agar phantom with mechanical inclusion. (e) B-mode structural image of the phantom. (f) Quantitative map of shear modulus computed from the dynamic shear wave visualization. (g) Linear fitting of phase delay versus position offset for two wave propagation paths. The shear modulus in the marked regions in (e) calculated using Eq. (15) is 2.9 and 17.1 kPa, respectively. Adapted from [180].

Surface wave imaging methods have been investigated in a wide range of applications, mainly for the detection of pathological or physiological changes, ranging from soft tissues such as the cornea [57, 63, 98–100, 102, 103, 105, 107, 109, 111, 113–115, 118], retina [186], brain [183], skin [71, 108, 120], kidney [112], fat and soft tissue tumors [97], and muscle [104], to relatively hard tissues such as cartilage [101, 106] and tendons [86]. In common with OCT, as described in this Special Issue, ophthalmology is a major application of OCE, where relatively low-scattering tissues, such as the cornea, allow imaging elastic waves at relatively high SNR. For example, Fig. 9 shows elastograms of the estimated Young's modulus of the cornea in two porcine eyes taken from the same animal, for which cornea 1 is untreated (control) and cornea 2 is treated by ultra-violet (UV) light-based cross-linking while cycling intra-ocular pressure (IOP) [187]. The data clearly indicate anisotropic characteristics, which become more pronounced at higher IOP. In another example, shown in Fig. 10, the phase velocity of the elastic wave was used to map depth-wise the distribution of corneal mechanical properties in a rabbit eye. This example highlights the benefit of structural imaging with OCT combined with mechanical characterization available from OCE in a combined image. We predict that such methods will find their first clinical applications in the assessment of therapeutic procedures on the cornea, such as laser-assisted *in situ* keratomileusis (LASIK) surgery [65] and UV light-based cross-linking of keratoconus-afflicted corneas [188].

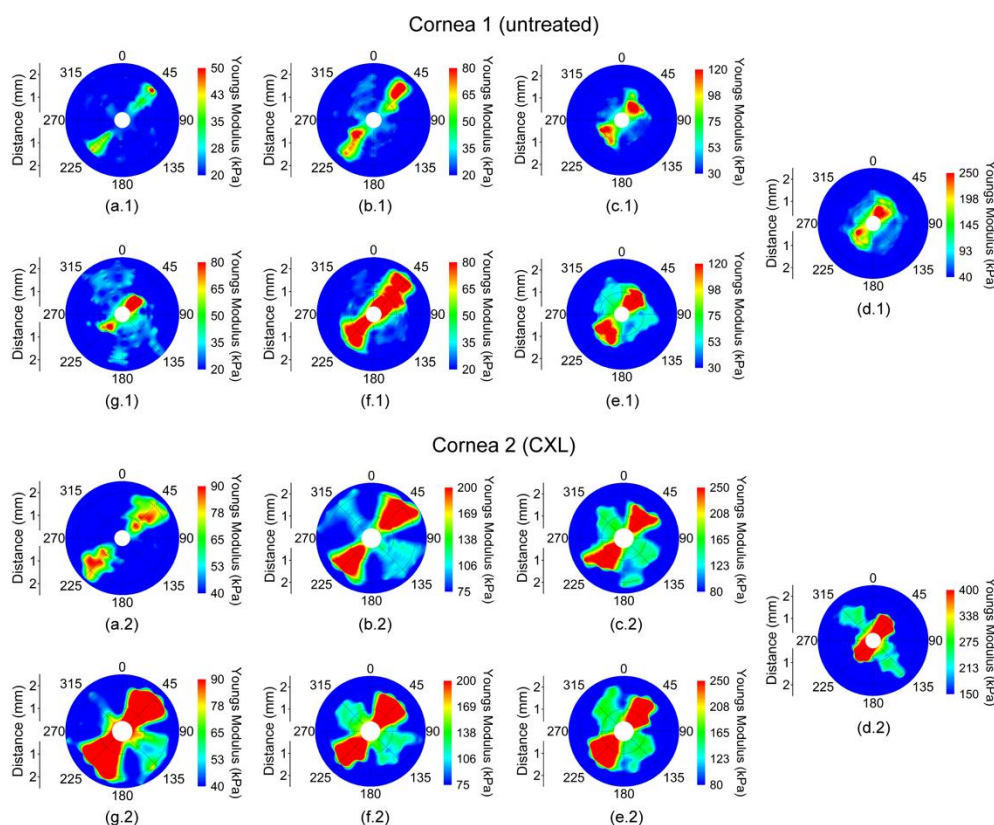


Fig. 9. Young's modulus maps in two porcine corneas from the same animal for increasing IOP: (a) 15, (b) 20, (c) 25, and (d) 30 mmHg; and at decreasing IOP: (e) 25, (f) 20, and (g) 15 mmHg. Cornea 1 was untreated and Cornea 2 was CXL-treated. Young's modulus scale is different for each IOP. Adapted from [187].

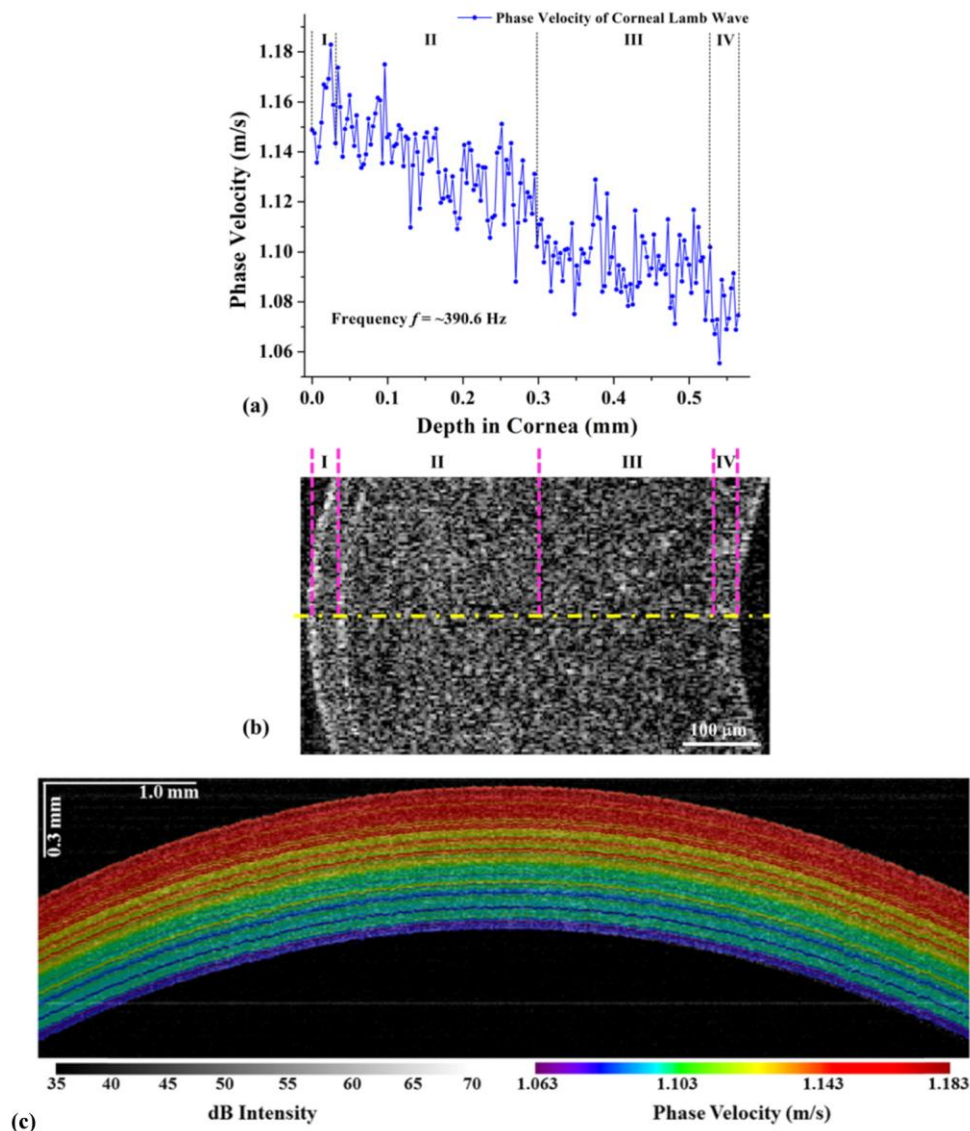


Fig. 10. (a) Elastic wave phase velocity versus depth indicating the distribution of corneal stiffness associated with the structural features indicated in (b), a cross-sectional OCT image. Region I: epithelium. Region II: anterior stroma. Region III: posterior stroma. Region IV: innermost region. (c) Combined two-dimensional depth-resolved micro-scale corneal elastography, revealing corneal layers. Adapted from [57].

Assessing tissue viscoelastic properties quantitatively by OCE is still at an early stage. As well as recognizing that viscosity is not accounted for in the simple approach [181], boundary conditions must be carefully considered in the conversion of elastic wave speed into quantitative values of tissue viscoelasticity. For example, finite-element modelling (FEM) supported by experimental data showed that taking account of the stress at the tissue surface, *e.g.*, imparted by a fluid, significantly reduced the group velocity of the elastic wave and, thus, could produce errors in quantification of elastic properties [109, 111]. Geometrical factors, such as tissue curvature and thickness, also have profound effects on the measured elastic wave speed [105]. Han *et al.* performed a systematic analysis of the accuracy of four analytical models and FEM for extracting the elastic modulus of soft samples [45]. The results

demonstrate that FEM is more robust than the analytical models, but requires extensive computation time. It has been shown that using the Rayleigh-Lamb frequency equation (relating the angular frequency to the phase velocity) to determine the Young's modulus provides the closest values to those provided by FEM and could be used for relatively rapid estimation of the elastic modulus.

Transient excitation methods, such as air puff or ARF, necessarily produce multiple frequencies in the induced elastic waves. Spectral decomposition can provide dispersion curves which could be used to extract both elastic and viscous properties of the sample [45, 57, 109, 110]. Such quantification requires application of either time-consuming FEM, or other analytical models, which are all constrained by specific assumptions [45], but may provide a more accurate and complete biomechanical assessment. Spectral decomposition of the elastic waves can also provide depth-resolved information due to the wavelength dependence of elastic wave penetration into the sample [70, 71, 117, 189]. Additionally, it allows for assessment of mechanical properties well beyond the OCT imaging depth, since the penetration depth of Rayleigh waves can reach many millimeters and even centimeters, depending on the wavelength [190]. This presents another opportunity to probe and identify the biomechanical properties of deep structures with OCE, in common with compressive methods [37, 69].

As described above, the lateral resolution of the elastic wave imaging methods is limited by the window size used for spatial phase gradient calculations to obtain the speed and wavelength of the elastic wave. On the other hand, *temporal analysis* of the tissue response to an external impulse allows highly localized assessment of tissue mechanical properties that is only limited by the resolution of loading and/or detection techniques, which can be, theoretically, as small as a few micrometers. The first such spatial elastographic maps, of inhomogeneous phantoms and partially cross-linked corneas, are presented in [188]. In temporal analysis methods, an external stimulus is used to remotely induce a displacement in the sample, and a phase-sensitive method, typically co-focused with the stimulus, is utilized to monitor the localized temporal response of surface deformations. Again, spectral decomposition can be used to quantify the viscoelasticity of the measured position [64, 191], as well as the depth-resolved viscoelasticity [64]. Wu *et al.* showed that spectral analysis of the displacement response of rabbit crystalline lenses of different ages in response to ARF *in situ* could reconstruct the lens viscoelasticity [191]. Expanding upon the displacement response spectral analysis, Wang *et al.* showed the feasibility of a utilizing the surface temporal displacement profile to distinguish layered phantoms [87], which, when combined with an analytical model [64], could provide the depth-resolved viscoelasticity distribution from only the surface temporal profile. Comprehensive experimental investigation is still required to demonstrate the best spatial resolution achievable with temporal analysis.

Most recently, an interesting approach has been adopted from ultrasound elastography, in which different harmonic continuous loading signals are simultaneously applied to opposite sides of the sample. Introducing very small difference in frequencies between the vibrational sources results in generation of a slowly moving "crawling wave" interference pattern [192]. This crawling wave approach to OCE significantly lowers the required imaging speed of fast-moving elastic waves and holds great promise for quantitative elastography of hard tissues without the need for ultra-fast sources.

7.2 Steady-state harmonic methods

In steady-state harmonic OCE, low-frequency vibrations are excited in tissue and regions of differing elasticity produce different vibration patterns [41, 78, 83]. If the external driving frequency matches a natural frequency of the sample, resonance will occur, which has been used for spatially mapping biomechanical properties based on the resonance frequency [38, 128, 130, 193]. Similarly, sweeping the amplitude modulation frequency of the ultrasound carrier in ARF can provide spectroscopic mechanical contrast in tissue, as shown in Fig. 11,

revealing the difference in mechanical properties of loose and dense fibrous caps in arterial walls, based on their resonance frequencies [91]. The extent to which the frequency responses of different regions within the tissue are coupled and how regional properties are affected by sample shape and properties of the boundary have largely yet to be explored (although the effect of sample geometry has been examined in [128, 130]), but computational models will undoubtedly be useful in assessing this. This coupling is to some extent avoided by a localized harmonic loading method, such as the magnetomotive method discussed in Section 5.

8. Additional opportunities and challenges

Throughout this review, we have highlighted opportunities and challenges as they arose. In this section, we consider several further issues that have not been covered so far.

There is no doubting the attractiveness of probing mechanical contrast or properties via intrinsic loading, as described at the end of Section 5. One such burgeoning non-OCE approach of great promise is Brillouin microscopy, as alluded to earlier [140, 194, 195]. OCE and Brillouin microscopy will continue to prove complementary, in the mechanical contrast they probe, the resolution and field of view they achieve, and the applications they are suited for.

Another intriguing intrinsic property is optical birefringence, which is reflected in both the molecular and organizational aspects of biological tissue. Birefringence is the source of contrast probed with polarization-sensitive OCT (PS-OCT) and relatively recently it has become possible to extract from volumetric PS-OCT images birefringence (equivalently differential retardation) as a parameter, instead of the related, but harder to interpret, parameter of cumulative retardation [158]. (In this regard, the extraction of strain and birefringence are related as parametric approaches to OCT [152].)

Birefringence can be altered by stress in various ways, and stress-induced birefringence in rigid non-biological materials has been explored with OCT [196]. In soft tissues, it has recently been shown that stress induces changes in the birefringence of airway smooth muscle [197]. There has also been one preliminary study comparing OCE and PS-OCT [198]. Such studies are intriguing and suggest future avenues of investigation to exploit the potential of PS-OCT to characterize stress in soft tissues, since stress is a parameter that, as explained elsewhere in this review, is exceptionally difficult to access.

Although viscoelasticity has been discussed in Section 6 [150] and Section 7 [45, 64, 109–111], it has featured necessarily little in this review, because there is little work explicitly focusing on the viscosity of soft tissue [150], although that is not the case for the wider field of optical elastography [182, 199].

There has been exceptionally little done to date in the area of validation of performance, whether of the technical performance of the methods, or validation of their performance in applications. Validation of technical performance requires the availability of appropriate phantoms, for example, which have been much less developed for mechanics than for optics [200]. Technical validation would also benefit from round-robin measurements of phantoms in different laboratories to establish performance parameters such as spatial and mechanical property resolution and range. For methods aspiring to quantitative performance, validation of computational approaches will also need to be included in this mix. For applications, the ultimate reporting of rigorously assessed sensitivity and specificity for diagnostic applications or accuracy assessments for specific mechanical property measurements will need to follow.

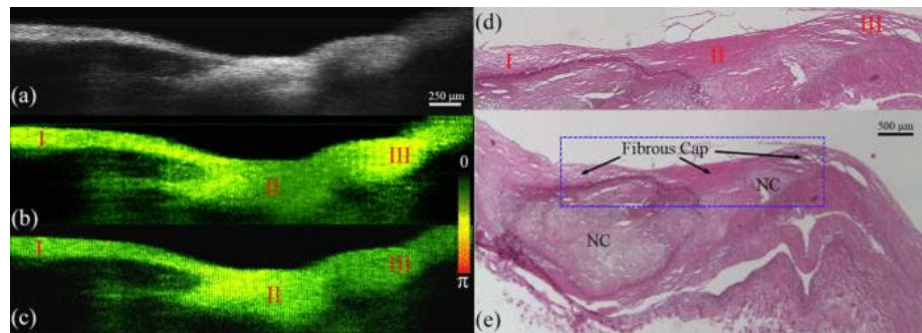


Fig. 11. Elastogram of human coronary artery produced by resonant acoustic radiation force OCE. (a) OCT structural image; (b) elastogram at 500 Hz driving frequency; (c) elastogram at 800 Hz driving frequency; (d) and (e) histology. Adapted from [91].

9. Conclusion

OCE has the advantage that it follows in the wake of the broader field of elastography, in which many of the variants of temporal and spatial variables of loading methods, and technologies to realize them, as well as soft tissue viscoelastic models and computational methods have been explored [7–9]. It is only in fairly recent years, since 2008, that this parameter space has begun to be explored in the context of OCE. This exploration must take into account the intrinsic differences in optics, of higher resolution, that alters the observable mechanical contrast, and of lower penetration, that enhances the sensitivity to surface effects, such as topography and friction (if contact is used). Although many OCE methods display mechanical contrast, not all do so on resolution scales that reach those expected of imaging optics, or yet do so on time frames that are suitable in applications, and although many claims are made for *quantitative* methods, there has been no rigorous validation of these claims, and the true picture is likely to be much more complex. Of course, the need for quantitation remains debatable, and must be assessed application by application. Already, as discussed herein, there are signs that some groups are moving beyond demonstrations of novelty, to systematic investigations of an application, such as intraoperative breast tumor margin identification [52, 151, 155] and monitoring therapeutic procedures on the cornea [115]. Undoubtedly, the field will continue to grow, as there are many remaining opportunities for novelty in methods; very little research done to date on probe design, such as would be suitable for endoscopy; combination of experimental data with models and computational methods to overcome artifacts and enhance accuracy is in its infancy; and there is a very large application space to explore. In order that the field does not remain an academic curiosity, we sincerely hope that at least one application takes off in the next few years.

Funding

This work was supported, in part, by: the U.S. National Institutes of Health (NIH) grants 2R01EY022362, 1R01HL120140; U.S. Department of Defense (DOD) Congressionally Directed Medical Research Programs (CDMRP) grant PR150338; and The Australian Research Council.

Acknowledgments

KL thanks his current and former lab members contributing to elastography project: Shang Wang, Jiasong Li, Manmohan Singh, Chen Wu, Zhaolong Han, Achuth Nair, Chih-Hao (Peter) Liu, Raksha Raghunathan, Stepan Baranov, and Kiran Manapuram. DS thanks former group members: Brendan Kennedy, Robert McLaughlin, Kelsey Kennedy, Lixin Chin, Andrea Curatolo, Rodney Kirk, Bryden Quirk, and Steven Adie, current group members: Philip Wijesinghe, Wes Allen, Qingyun Li, and Karol Karnowski, and visitor Gijis van Soest.